Spatiotemporal expression of regulatory kinases directs the transition from mitosis to cellular morphogenesis

Shuo Yang[1], Jennifer McAdow[1], Yingqiu Du[1], Jennifer Trigg[2], Paul H. Taghert[2], and Aaron N. Johnson[1,3]

[1]Department of Developmental Biology
[2]Department of Neuroscience
Washington University School of Medicine
St. Louis, MO 63110

[3]Author for correspondence: anjohnson@wustl.edu
Running Title: Bsd activates Polo during myogenesis

Abstract

Embryogenesis depends on a tightly regulated balance between mitosis, differentiation, and morphogenesis. Understanding how the embryo uses a relatively small number of proteins to transition between growth and morphogenesis is a central question of developmental biology, but the mechanisms controlling mitosis and differentiation are considered to be fundamentally distinct. Here we show the mitotic kinase Polo, which regulates all steps of mitosis [1-3], also directs cellular morphogenesis after cell cycle exit. In mitotic cells, the Aurora kinases activate Polo to control a cytoskeletal regulatory module that directs cytokinesis [4-6]. We show that in the post-mitotic mesoderm, the control of Polo activity transitions from the Aurora kinases to the uncharacterized kinase Back Seat Driver (Bsd), where Bsd and Polo cooperate to regulate muscle morphogenesis. Polo and its effectors therefore direct mitosis and cellular morphogenesis, but the transition from growth to morphogenesis is determined by the spatiotemporal expression of upstream activating kinases.

Introduction

Rapid cell divisions are the hallmark of early embryonic development, but as development proceeds cells will exit the cell cycle to acquire specialized, functional morphologies. Tissue patterning through the differential expression of morphogens is a well-understood developmental process. On the other hand, kinases are generally considered to be stably expressed mediators of upstream activating proteins [7-11], and most kinases are ubiquitously expressed while the embryo is undergoing rapid cell divisions (Fig. S1A, Table S1). However, during tissue diversification and organogenesis, the expression of many kinases becomes enriched or depleted in specific tissues (Fig. S1A, Table S1). The spatiotemporal regulation of kinase expression could be a previously unrecognized and essential mechanism that drives the transition from mitosis to cellular morphogenesis.

Mitosis is controlled by two sets of kinases. Cyclin dependent kinases regulate progress through the cell cycle, and mitotic kinases, including Aurora kinases and Polo-like kinases (Plks), direct mitotic entry, chromosome segregation, and cytokinesis [12-17]. Plk activity is dependent on two conserved protein domains. The C-terminal Polo-Box Domain (PBD) recognizes target substrates, and PBD docking enhances substrate phosphorylation by the Kinase Domain (KD)[17]. Intramolecular interactions between the PBD and the KD dictate the affinity of Polo for specific substrates. The PBD of *Drosophila* Polo kinase (Polo) binds the microtubule protein Map205 during interphase, which effectively sequesters Polo on microtubules [18]. During mitotic entry, activating phosphorylation of the KD by Aurora B (AurB) relieves PBD binding to Map205 and promotes PBD binding to pro-mitotic substrates and structures [4]. A similar regulatory mechanism has recently been proposed to modulate Polo activity during meiosis [19]. In addition, when Polo is inactive, intramolecular binding between the Polo KD and the PBD masks a nuclear localization signal (NLS). Activating phosphorylation exposes the NLS, allowing Polo to enter the nucleus prior to nuclear envelope breakdown [20]. Although Aurora-mediated Polo activation is an essential regulatory step during cell division, the role of Polo in post-mitotic tissues, if any, is unknown.

Cellular morphogenesis provides functionality for highly specialized cells, and morphogenesis generally initiates after cells have exited the cell cycle. Cellular guidance is a cytoskeleton-dependent morphogenetic process in which a post-mitotic cell generates long projections that interact with or connect to other cells. Axon guidance is perhaps the most studied form of cellular guidance, and provides the foundation for connecting neurons throughout the nervous system [21]. Nascent myotubes, which are immature post-mitotic muscle precursors, also undergo cellular guidance and extend bipolar projections to connect

with the tendon precursors that attach to the skeleton [22](Movie 1). The body wall muscles in *Drosophila* are easily visualized in live, unperturbed embryos [23, 24], and have served as an essential model to understand the cellular and molecular mechanisms that direct muscle development [23-30]. The transmembrane receptors Heartless, Kon-tiki, and Robo regulate myotube guidance in *Drosophila* by transducing the navigational signals that direct myotube leading edges toward tendon precursors [23, 28, 30]. However, the intracellular pathways that link guidance receptors with the cytoskeletal changes underlying muscle morphogenesis are poorly understood.

Here we report a novel function for Polo in the post-mitotic mesoderm, where Polo regulates cellular morphogenesis. The embryonic mesoderm undergoes multiple rounds of cell division after gastrulation, and mitosis in the mesoderm is largely complete by Stage 12. Nascent myotubes exit the cell cycle and begin myotube guidance during Stage 12, but surprisingly we found Polo is activated in the post-mitotic mesoderm during myotube guidance. Aurora kinases are the known activators of Polo, but the Aurora kinases were expressed in the embryonic mesoderm only until Stage 10. In contrast, the expression of the kinase Back seat driver (Bsd) was enriched in the Stage 12 mesoderm, where Bsd promoted Polo activation and directed microtubule reorganization necessary for myotube guidance. Thus the transition from mitosis to cellular morphogenesis is achieved through the spatially and temporally restricted expression of the Aurora kinases and Bsd. The Polo orthologue Plk1 was activated by the Bsd orthologue Vrk3 in mammalian cells, arguing Bsd regulates a conserved intracellular signaling pathway that directs muscle morphogenesis.

Results

We carried out a forward genetic screen to identify regulators of myotube guidance, and uncovered a mutation in *CG8878* that disrupted muscle development. The body wall muscles in *CG8878* embryos showed pronounced navigational defects, so we named the gene *back seat driver* (*bsd*) (Figs. 1A-E, S1B). The allele recovered from our screen (hereafter bsd^1) is an embryonic lethal nonsense mutation (Q545*) that is predicted to produce a C-terminal truncation (Fig. 1C). *bsd* encodes a conserved serine/threonine kinase orthologous to the Vaccinia Related Kinases (VRKs), and proteins in the VRK family contain a single conserved kinase domain (KD) near the N-terminus, and a highly variable C-terminus (Figs. 1C, S1C,D). The Bsd paralog Ballchen (Ball) regulates sarcomere assembly in adult flight muscles, but the null allele $ball^2$ is embryonic viable [31], suggesting Ball is not a major regulator of embryonic muscle development. Vertebrate VRK proteins have not been shown to regulate myogenesis, but pathogenic VRK1 variants have been identified in patients with motor neuropathies that may arise from defects in cellular morphogenesis [32].

Bsd directs myotube guidance

Thirty distinct muscles develop per embryonic hemisegment in *Drosophila*, and each muscle acquires a specific morphology (Fig. 1A,B). Myogenesis initiates with the specification of founder cells, which are muscle precursors with unique identities that form individual embryonic muscles. After specification, post-mitotic muscle founder cells break symmetry to begin elongation, and concurrently fuse with neighboring fusion competent myoblasts to form syncytial myotubes [25]. The nascent myotubes will elongate and identify muscle attachment sites on tendon cells in the ectoderm. The correct elongation and attachment of an individual muscle establishes a stereotypical morphology, and forms the largely invariant musculoskeletal pattern in abdominal segments A2-A8 (Fig. 1A,B). To broadly quantify morphology defects we used an antibody against Tropomyosin to visualize muscle shape ~~at the end of myogenesis~~, and found a majority of the thirty muscles in each hemisegment showed significant morphology defects in bsd^1 embryos (Figs. 1A,B, S1E).

To understand the myogenic role of Bsd in more detail, we used cell identity reporters to assay founder cell specification, myoblast fusion, and myotube guidance as previously described [23]. *5053.Gal4* is active in one founder cell that gives rise to the Ventral Lateral 1 (VL1) muscle, and *slou.gal4* is active in five founder cells that give rise to the Dorsal Transverse 1 (DT1), the Longitudinal Oblique 1 (LO1), the Ventral Acute 1 (VA1), the Ventral Acute 3 (VA3), and the Ventral Transverse 1 (VT1) muscles. *5053.Gal4* and *slou.gal4* expressing founder cells were correctly specified in *bsd* embryos (Fig. S1F), but myotube elongation and muscle

attachment site selection, which are the two hallmarks of myotube guidance, were significantly disrupted (Fig. 1D-G, Movie 1). In contrast, tendon cells developed normally in *bsd* embryos (Movie 2), suggesting the myotube guidance defects we observed are not secondary to tendon cell fate specification or tendon cell positioning. We also found that the initial round of myoblast fusion was modestly reduced in *bsd* embryos (*bsd* fusion index=85.7%; Fig. 1H), although not to the degree reported for other well-characterized fusion mutants such as *loner* [29]. Bsd is thus an essential regulator of muscle morphogenesis that directs myotube guidance and, to a lesser extent, myoblast fusion.

Bsd acts cell autonomously in the mesoderm

We generated and validated an antibody against Bsd (Fig. S2A-C), and found Bsd was ubiquitously expressed in blastoderm embryos (Fig. S2D). However, after gastrulation, Bsd expression was more dynamic. Founder cells are specified during Stages 10-11, and Bsd expression in the mesoderm during Stage 11 was reduced compared to subsequent stages of myogenesis (Figs. 2A, S2D-F). Myotube guidance begins at Stage 12, and Bsd expression levels in the mesoderm peaked during Stages 12-14 (Figs. 2A, S2D-F). Myotube guidance is complete by Stage 16, and the relative levels of Bsd expression in the mesoderm were reduced in Stage 16 embryos (Figs. 2A, S2D-F). The Bsd expression pattern is consistent with our hypothesis that kinase expression is spatially and temporally regulated during embryogenesis.

The temporally dynamic expression of Bsd in the mesoderm suggested Bsd functions cell autonomously to regulate muscle morphogenesis. ~~Indeed,~~ *bsd*^{1} embryos that expressed wild-type Bsd in the mesoderm under the control of *24B.Gal4* showed a largely normal muscle pattern (Fig. 2B-D). Proteins in the VRK family contain a highly conserved ATP binding pocket that is essential for catalytic activity [(Fig. S1D), [33]], and our computational structural models predicted that Bsd isoleucine 129 binds ATP (Fig. 2E). *bsd*^{1} embryos that expressed ~~the predicted kinase-dead~~ Bsd.I129A in the mesoderm showed a myogenic phenotype that was indistinguishable from *bsd*^{1} embryos (Fig. 2B-D), arguing Bsd kinase activity is required for proper muscle morphogenesis.

Bsd activates Polo to direct muscle morphogenesis

To uncover Bsd effectors during myotube guidance, we used recombinant Bsd to precipitate Bsd interacting proteins from whole embryo lysates, which were then sequenced by Mass Spectrometry (MS; Figs. 3A, S3A). The MS results identified over 150 candidates that interacted with Bsd, none of which were known to regulate muscle morphogenesis (Table S2). Since the absolute quantity of each candidate in the input embryo lysate was not known, the relative abundance of a candidate in the pool of precipitated proteins could not be used to

prioritize the potential Bsd-interacting proteins. To rank the candidates for further analysis, we first validated protein-protein interactions in S2 cells, and then characterized muscle morphogenesis in embryos with reduced candidate gene function. The mitotic kinase Polo showed the strongest interaction with Bsd in S2 cells (Fig. S3B), and we confirmed the interaction with reciprocal immunoprecipitation experiments (Fig. 3B,C). Strikingly, the Bsd.Q545* protein encoded by our EMS-induced *bsd*^{1} allele did not interact with Bsd (Fig. 3B,C). Embryos homozygous for the hypomorphic alleles *polo*^{1} and *polo*^{KG03033} showed myogenic phenotypes similar to *bsd* embryos (Fig. S3C,D). We tested four candidates in addition to Polo, and although these proteins showed a weak interaction with Bsd in S2 cells (Fig. S3B), we could not confirm muscle phenotypes with alleles that affected the remaining candidates. Polo was thus the highest-priority candidate for further analysis.

Germ line clones of the hypomorphic allele *polo*^{1} reduce the maternal contribution of Polo, and *polo*^{1} maternal mutant embryos showed defects in mitotic chromosome alignment [34]. However, *polo*^{1} zygotic mutants with a normal maternal contribution of Polo were largely viable, and did not show embryonic mitotic defects [35]. After gastrulation, the mesoderm undergoes four rounds of cell division that conclude by Stage 11 [36]. During Stages 10-11, each founder cell is specified from a pool of cells known as an equivalence group. The remaining cells in the equivalence group then differentiate into fusion competent myoblasts [25]. To understand if *polo*^{1} zygotic mutant embryos undergo normal cell divisions prior to founder cell specification, we quantified the number of Mef2-positive somatic mesoderm cells in Stage 10 embryos. Although *polo*^{1} embryos showed a 14.2% decrease in the number Mef2-positive cells compared to wild-type embryos (Fig. S3E,F), the number of *5053.Gal4* and *slou.gal4* expressing founder cells were not significantly different between wild-type and *polo*^{1} Stage 12 embryos (Fig. S3G,H). These observations suggest that the mitotic defects in *polo*^{1} zygotic mutant embryos do not appreciably affect equivalence group size or founder cell specification. Using *5053.Gal4* and *slou.gal4* to characterize muscle morphogenesis, we identified myotube elongation and muscle attachment site selection defects in the VL1, DT1, LO1, and VT1 muscles of *polo*^{1} embryos (Fig. 3D,E), suggesting Polo directs myotube guidance after founder cell specification. Importantly, the severity of muscle morphogenetic defects was equivalent among *bsd*^{1}, *polo*^{1}, and *bsd*^{1} *polo*^{1} embryos, arguing Bsd and Polo act in a common pathway to direct myotube guidance (Figs. 3F-H, S3I).

Since Bsd and Polo are both protein kinases, we used phosphorylation assays to understand if one protein might act upstream of the other. A common strategy for measuring protein phosphorylation is to immunoprecipitate target proteins, and assay total phosphorylation

by Western Blot. Bsd is a predicted serine/threonine kinase, and Polo isolated from S2 cells transfected with wild-type Bsd had significantly more phosphorylated threonine than controls (Figs. 4A, S4A). However, Polo isolated from cells transfected with kinase-dead Bsd.I129A did not show a significant change in the threonine phosphorylation (Fig. S4B). Polo is activated by phosphorylation of Thr182 [6], so we repeated our phosphorylation assay with an antibody that specifically recognizes $Polo^{pThr182}$ and found Bsd significantly increased $Polo^{pThr182}$ levels (Figs. S4C,D). Activated $Polo^{pThr182}$ translocates to the nucleus [20], and Bsd promoted the nuclear translocation of wild-type Polo but not phospho-dead Polo.T182A in S2 cells (Fig. 4B,C). These S2 cell studies suggested Bsd phosphorylates Polo, so we performed cell-free kinase assays and found Bsd phosphorylated Polo on Thr182 (Fig. S4E). Together our data argue that Polo is a direct substrate of Bsd kinase activity.

To understand how Polo activity is regulated *in vivo*, we assayed Polo phosphorylation in whole embryo lysates and found Bsd broadly promoted Polo phosphorylation on threonine residues (Fig. 4D). Similar to Bsd expression (Fig. 2A), activated $Polo^{pThr182}$ levels were dynamic in the mesoderm, and significantly increased during Stage 12 (Figs. 4E,F S4F). However, in *bsd*^{1} embryos, $Polo^{pThr182}$ levels did not change during Stage 12 (Figs. 4E,F S4F), despite the fact that Polo protein levels were comparable between wild-type and *bsd*^{1} embryos (Fig. S4F). Functionally, *bsd*^{1} embryos that expressed activated Polo.T182D in the mesoderm under the control *Mef2.Gal4* showed improved muscle morphogenesis compared to *bsd*^{1} embryos (Fig. 4G). Bsd therefore directs Polo activation in the mesoderm of Stage 12 embryos, and Bsd-mediated Polo activation is required for myotube guidance.

Aurora kinases are not expressed in the post-mitotic mesoderm

Nascent myotubes exit the cell cycle and begin myotube guidance during Stage 12 (Fig. S5A), so it was surprising that a mitotic kinase like Polo was activated in the post-mitotic mesoderm (Fig. S4F). The pro-mitotic Aurora kinases are the only known activators of Polo or its vertebrate orthologue Plk1 [20, 37]. *aurora A* (*aurA*) and *aurora B* (*aurB*) were broadly expressed in the mitotic mesoderm until Stage 10, but by Stage 12 *aurA* and *aurB* expression was undetectable in the somatic mesoderm (Figs. 5A-C, S5A,B). Alternatively, Bsd expression was enriched in the mesoderm during Stage 12 (Fig. 2A), suggesting the control of Polo activation transitions from the Aurora kinases to Bsd during myotube guidance. To test this model, we assayed $Polo^{pThr182}$ levels in the mesoderm of Stage 12 *aurA* and *aurB* embryos, and found $Polo^{pThr182}$ levels were not significantly different between mutant and control embryos (Fig. 5D). In addition, *aurA* and *aurB* embryos showed normal muscle morphology at the end of

embryogenesis (Fig. S5C,D). These data further suggest the control of Polo activation transitions from the Aurora kinases to Bsd during myotube guidance.

We next asked why it might be necessary for Bsd to regulate Polo activity in place of AurA and AurB. The Aurora kinases regulate multiple mitotic proteins in addition to Polo/PLK1 [38], and we hypothesized that Aurora kinase expression is reduced after Stage 10 to promote cell cycle exit in the mesoderm. We used *Mef2.Gal4* to temporally misexpress *aurB* in the mesoderm, and found *Mef2>aurB* embryos had significantly more mitotic cells than controls (Fig. S5E-G). AurB specifically promotes the transition from S phase to the G2/M phase of the cell cycle [39], and *Mef2>aurB* embryos had significantly more mesoderm cells in the G2/M phase than control embryos (Fig. 5E,F). Functionally, *Mef2>aurB* muscles had more myonuclei at the end of myogenesis than controls (Fig. S5H,I), arguing extended mitosis in the mesoderm produced more myogenic precursors. Thus the control of Polo activity during myotube guidance transitions away from the Aurora Kinases to promote cell cycle exit.

Polo effectors Tum and Pav direct myotube guidance

How then does Bsd-activated Polo regulate myogenesis? Two *Drosophila* Polo effector proteins, the GTPase activating protein Tumbleweed (Tum) and the kinesin microtubule motor protein Pavarotti (Pav), coordinate cytoskeletal dynamics to position furrow formation at the onset of cytokinesis [5, 40, 41]. Polo directly interacts with Tum, Tum directly interacts with Pav, and Polo is required for the correct localization of Tum and Pav during cytokinesis [5, 42]. In addition, a role for Tum in myotube guidance was suggested in studies showing Tum regulates the microtubule cytoskeleton to direct myotube elongation [27]. The Polo/Tum/Pav cytoskeletal regulatory module that directs cytokinesis may therefore be reactivated in the post-mitotic mesoderm to direct microtubule reorganization during myotube guidance. To extend previous work, we reanalyzed muscle morphogenesis in *tum* embryos using the cell identity reporters *5053.Gal4* and *slou.gal4*, and found Tum directs both myotube elongation and muscle attachment site selection during myotube guidance (Fig. 6A,B; Movie 3). In addition, the severity of muscle morphogenetic defects was equivalent among $polo^{1}$, tum^{DH15}, and $polo^{1}$ tum^{DH15} embryos (Fig. S6A,B). pav^{B200} embryos also showed muscle phenotypes, and the severity of muscle morphogenetic defects was equivalent among tum^{DH15}, pav^{B200}, and tum^{DH15} pav^{B200} embryos (Fig. S6C). These genetic studies suggest Polo, Tum, and Pav act in a common myogenic pathway, and argue Bsd reactivates the Polo/Tum/Pav cytoskeletal regulatory module to direct myotube guidance.

Bsd regulates the microtubule cytoskeleton

The microtubule cytoskeleton transitions from a cortical organization in founder cells to a linear organization in nascent myotubes that parallels the axis of elongation (Movie 4)[27]. Live imaging of microtubule reorganization revealed that the microtubule transition was delayed by over 60min in *bsd* myotubes, and that *bsd* myotubes failed to maintain linear microtubule arrays (Fig. 6C,D; Movie 4). However, the actin cytoskeleton was largely unaffected in *bsd* myotubes (Fig. S6D). The microtubule minus-end nucleator γ-tubulin initiates the assembly of new microtubules [43], and at the onset of myotube elongation γ-tubulin foci are predominantly localized to the myotube cortex [27]. As the microtubule cytoskeleton transitions to linear arrays, γ-tubulin foci appear in the internal myotube cytoplasm through a Tum-dependent mechanism (Fig. 6E,F)[27]. In bsd^1 embryos, γ-tubulin foci failed to accumulate in the myotube cytoplasm, suggesting Tum-dependent γ-tubulin mediated microtubule nucleation is defective in *bsd* myotubes (Figs. 6E,F S6E,F). Bsd is thus an essential regulator of the microtubule cytoskeleton.

Bsd and Polo orthologues regulate muscle morphogenesis

To understand if the regulatory functions of Bsd are conserved, we used small interfering RNAs (siRNAs) to knock down Vrk1, Vrk2, and Vrk3 during mammalian muscle morphogenesis. Under culture conditions that promote differentiation, C2C12 cells (immortalized mouse myoblasts) will form nascent myotubes that extensively elongate [44]. C2C12 cells treated with Vrk1 and Vrk2 siRNAs were morphologically similar to control treated cells after 7 days of differentiation (Fig. S7A,B), but C2C12 cells treated with Vrk3 siRNAs showed significantly reduced elongation and a reduced fusion index (Figs. 7A-D, S7A-D). These myogenic assays functionally confirmed our phylogenetic analysis, arguing Bsd is most similar to Vrk3 (Fig. S1C). Post-mitotic C2C12 cells treated with the Plk1 inhibitor Volasterib phenocopied C2C12 cells treated with Vrk3 siRNAs (Fig. 7A-D). In addition, Vrk3 physically interacted with Plk1 (Fig. 7E) and promoted activating phosphorylation of Plk1 in HEK293 cells (Fig. 7F). Thus the Bsd orthologue Vrk3 activates the Polo orthologue Plk1 in mammalian cells. In addition, bsd^1 embryos that expressed Vrk3 in the mesoderm showed largely normal muscle morphology (Fig. 7G). Our results argue that the functions of Bsd and Vrk3 are highly conserved.

Discussion

This study identified Bsd as a conserved regulator of Polo activation. Bsd promoted Polo phosphorylation in cultured cells and in cell-free kinase assays (Fig. 4A), and Bsd was required to activate Polo in the post-mitotic mesoderm (Figs. 4E, S4E). In addition, activated Polo (Polo.T182D) rescued the *bsd* myogenic phenotype (Fig. 3F), which argues an essential function of Bsd during myotube guidance is to activate Polo. The microtubule cytoskeleton reorganizes to drive morphological changes in nascent myotubes, and Bsd directed microtubule reorganization during myotube guidance (Fig. 6C-F; Movie 4). These observations are consistent with a model in which Bsd activates a Polo/Tum/Pav cytoskeletal regulatory module to direct cellular morphogenesis (Figs. 7H, S7E).

We have also identified an example in which the dynamic expression of regulatory kinases directs the transition from mitosis to cellular morphogenesis. The Aurora kinases are broadly expressed in the mitotic mesoderm, where they presumably activate Polo and other target proteins to initiate mitotic entry and complete the critical steps of mitosis (Fig. 5A). The Aurora kinases are not expressed in the post-mitotic mesoderm, and the temporal misexpression of AurB prolonged cell division in the mesoderm (Fig. 5E,F). Bsd expression was complementary to the Aurora kinases (Figs. 2A, 5A-C), and Bsd activated Polo in the post-mitotic mesoderm to direct muscle morphogenesis (Figs. 4E-G). Over 50% of the *Drosophila* kinases with known embryonic expression patterns transition from ubiquitous expression before gastrulation to tissue specific expression after gastrulation, and an additional 20% of kinases show spatially restricted expression throughout development (Table S1, Fig. S1A). Zebrafish kinases show similar embryonic expression patterns (Table S1, Fig. S1A). The dynamic expression of protein kinases in both invertebrates and vertebrates suggest that expression-based regulation of kinase signaling pathways could be broadly employed to direct the key events of embryogenesis.

Polo was reactivated in the post-mitotic mesoderm (Fig. S4F), which suggests Polo activity alone is not sufficient for mesodermal cells to enter mitosis. On the other hand, ectopic AurB expression in the mesoderm increased the proportion of cells in the G2/M phase of the cell cycle (Fig. 5E,F). Since AurB and Bsd activate Polo by phosphorylating Thr182 (Fig. 4E)[19, 20], AurB likely induces cell cycle progression through a Polo Thr182-independent mechanism. Cyclins are key regulators of the cell cycle, and the regulation of cyclin activity is best understood at the level of protein expression. However, the G2/M checkpoint regulator Cyclin B (CycB) can be detected throughout the cell cycle [45]. At the G2/M checkpoint CycB activity is phosphorylation dependent, where active CycB is phosphorylated on residues near the nuclear

export sequence and also dephosphorylated by Cdc25 on residues near the N-terminus [46]. In the *Drosophila* germline AurB promotes the phosphorylation of CycB [45], and in human lymphoma cells AurB increases the proportion of cells in G2/M [39]. AurA also activates CDC25 [38], which further implicates Aurora kinases as Polo/PLK1-independent regulators of cell cycle progression. Our studies argue that the control of the Polo transitions from the Aurora kinases to Bsd so that the Polo/Tum/Pav cytoskeletal regulatory module can be reactivated in differentiating, post-mitotic myotubes without promoting mitotic entry.

Bsd regulates myotube elongation and muscle attachment site selection (Movie 1), which are the hallmarks of myotube guidance. Our myotube guidance hypothesis argues that extracellular guidance cues, such as FGFs, corroborate with contact dependent interactions between myotubes and tendons to pattern the musculoskeletal system [23, 47]. The Bsd paralog Ball is phosphorylated during female meiosis where it functions to maintain spindle integrity [48]. Similar to Ball, Bsd might be phosphorylated and activated by an upstream kinase. Our MS experiment identified Par-1, Target of Rapamycin, and SR Protein Kinase (SRPK) as potential upstream kinases that could activate Bsd (Table S2). Mammalian SRPK1 was identified in a screen for tumor cell migration [49], and has been implicated in breast, lung, and renal cancer metastasis suggesting SRPKs promote the cytoskeletal changes necessary for cellular migration and cellular guidance [49-51]. Although *Drosophila* SRPK has not been linked to the extracellular receptors known to regulate myotube guidance, murine *Srpk3* is a Mef2 target gene in striated muscle [52], and SRPK proteins regulate developmental signaling pathways [53]. We favor a model in which an intracellular effector, such as SRPK, transduces guidance cues from the cell surface to activate Bsd and direct myotube elongation toward muscle attachment sites.

We found that activated Polo partially rescued the bsd^1 embryonic phenotype (Fig. 4G). While the levels of activated Polo in the rescue experiment may not have recapitulated endogenous levels of activated Polo, it is also possible that Bsd regulates Polo-independent pathways. For example, we validated a physical interaction between Bsd and the Myosin VI protein Jaguar (Jar; Fig. S3B). Jar stabilizes interactions between the actin and microtubule cytoskeletons [54], and is required for cell migration [55] and cellular guidance [56]. Although one essential role for Bsd is to activate the Polo/Tum/Pav cytoskeletal regulatory module, it seems likely that Bsd regulates additional cytoskeletal proteins, such as Jar, to direct myotube guidance.

Polo directs spindle formation, cytokinesis, and myotube guidance by regulating the microtubule cytoskeleton. The $polo^1$ allele was originally identified as a maternal effect mutation

that disrupted mitotic chromosome alignment [34], and Polo was later found to recruit γ-tubulin and Abnormal spindle protein (Asp) to the centrosome for microtubule nucleation [57]. The role of Polo during spindle assembly appears to be Tum and Pav independent, but during cytokinesis the Polo/Tum/Pav regulatory module uses the central spindle microtubules to position the contractile ring and initiate furrow formation [5, 58, 59]. We found that Bsd directs microtubule reorganization during myotube guidance, which may involve the recruitment of γ-tubulin to sites of microtubule nucleation (Fig. 6C-F). Tum also regulates myotube guidance (Fig. 6A,B), and is required for γ-tubulin localization in post-mitotic myotubes [27]. The precise mechanism by which Bsd and the Polo/Tum/Pav cytoskeletal regulatory module interact to direct myotube guidance remains unclear, but Tum and Pav appear to function outside of the nucleus to direct changes to the microtubule cytoskeleton in post-mitotic cells [27]. One possibility is that Bsd-activated Polo translocates to the myonucleus to direct the nuclear export of Tum and Pav after founder cells and fusion competent myoblasts have exited the cell cycle. Cytoplasmic Tum/Pav complexes would in turn reorganize the microtubule cytoskeleton to direct myotube elongation. Tum and Pav also regulate axon guidance in post-mitotic neurons [60], so understanding if Polo directly phosphorylates Tum and Pav to regulate the subcellular localization of the Tum-Pav complex may inform our overall understanding of cellular guidance. We predict that the Polo/Tum/Pav cytoskeletal regulatory module functions in many cell types to regulate tissue morphogenesis.

Mammalian Vrk3 regulated myotube elongation, physically associated with Plk1, and promoted activating phosphorylation of Plk1 (Fig. 7A-F). The active site in human VRK3 is divergent at three residues, which led to the hypothesis that VRK3 is a pseudokinase [61]. However, subsequent studies show that VRK3 has kinase activity under certain contexts [62], and our studies support an active role for Vrk3 in promoting phosphorylation (Fig. 7E). Although myotube guidance has not been studied in vertebrate systems, Plk1 was recently shown to regulate myogenesis in mice. Muscle-specific deletion of *Plk1* blocked limb muscle development during embryogenesis, and prevented muscle stem cells from activating after injury [63]. It remains unclear if Vrk3 activates Plk1 during mammalian muscle development, if the targets of Plk1 in the muscle lineage have been conserved, or if Plk1 regulates myofiber morphogenesis. Our study highlights the exciting possibility that the role of Plk1 during vertebrate muscle development and regeneration extends beyond the mitotic events of myoblast proliferation and muscle stem cell activation.

Methods

Drosophila genetics

The *bsd*^{1} allele was recovered in an EMS screen as described [24]. The following stocks were obtained from the Bloomington Stock Center: *aurA*^{1}, *jar*^{322}, *lost*^{1}, *polo*^{1}, *polo*^{KG03033}, *tum*^{DH15}, *pav*^{B200}, *Df(2R)BSC199*, *Df(2R)BSC699*, *Df(3L)BSC447*, *Df(2L)Exel7049, P{UAS-nod.GFP}, P{Gal4-tey*^{5053A}*}, P{GMR40D04-GAL4}attP2* (*slou.Gal4*)*, P{GMR57C12-GAL4}attP2* (*nau.Gal4*)*, P{Gal4-how*^{24B}*}, P{UASp-aurB.PrA}, P{UAS-eGFP}, P{UAS-Lifeact-RFP}, P{UAS-polo.T182D}, P{PTT-GC}polo*^{CC01326} (Polo-GFP)*,* and the FUCCI lines *P{UAS-GFP.nE2f1.1-230 }* and *P{UAS-RFP.CycB.1-266}.* The remaining stocks used in this study were *aurB*^{1689} [45], *P{Gal4-kirre*^{rP298}*}* and *P{kirre*^{rP298}*.nlacZ}* [64], *P{Gal4-Mef2}* [65], and *P{MHC.*τ*GFP}* [29]. *Cyo, P{Gal4-Twi}, P{2X-UAS.eGFP}; Cyo, P{wg.lacZ}; TM3, P{Gal4-Twi}, P{2X-UAS.eGFP}; and TM3, P{ftz.lacZ}* balancers were used to genotype embryos.

Bsd transgenic flies were generated by subcloning the *bsd* coding sequence (LD23371, *Drosophila* Genomics Resource Center, supported by NIH grant 2P40OD010949) into pUASt-Attb (KpnI/XbaI). Site directed mutagenesis by PCR sewing was used to make UAS.Bsd.I129A. Plasmids and P(acman) BACs (CH321-61F090 and CH322-02P20) were injected and targeted to a ϕC31 integration site at 22A2 (Rainbow Transgenic Flies; Bloomington Stock 24481); stable insertions were identified by standard methods.

RNA sequencing and variant identification

Total RNA was collected from 12-24hr embryos per manufacturer's specification (RNeasy kit, Qiagen). cDNA libraries were generated with the TruSeq stranded mRNA sample library kit (Illumina) and sequenced using 50bp paired-end reads on the Illumina HiSeq 2000 system. Two technical replicates of *w*^{1118} and *bsd*^{1} were prepared and sequenced. Sequence reads were mapped to the *Drosophila* genome with Genomic Short-Read Nucleotide Alignment Program (GSNAP) using the Cufflinks method. Variants (single nucleotide variants and insertions/deletions) were identified with the Broad Institute's Genome Analysis Toolkit (GATK), and the resulting variants were functionally tested by complementation test. The *bsd*^{1} allele (Q545*) was confirmed by Sanger sequencing.

Bsd antibody

We created a fusion Bsd::6xHis fusion protein by PCR, using the C-terminus amino acids 705–1004 of Bsd. We sub-cloned the 598bp fragment into the pHO4d 6xHIS expression vector [66] via conventional restriction enzyme sites. The Bsd 6xHIS fusion construct was transformed into competent BL21 (DE3) pLysS *E. coli* cells (Invitrogen) and grown, overnight shaking at 37°C in DYT supplemented with 100 µg/ml ampicillin. The cells were diluted 25 times

in fresh DYT media and grown at 37°C to an OD_{600}=0.6–0.7. We added isopropyl β-D-thiogalactoside (IPTG) to 1 mM to induce expression of the fusion protein and incubated overnight shaking at 18°C. We purified the 6xHIS fusion protein on nickel-nitrilotriacetic acid agarose (Qiagen, Valencia, CA) according to the manufacturer's protocols, under native conditions with modified buffers and dialyzed against PBS. We sent the purified protein to Pocono Rabbit Farm & Laboratory (Canadensis, PA) for guinea pig custom polyclonal antibody production.

Plasmids and mutagenesis

Expression plasmids for the immunoprecipitation screen were the BDGP Flag-HA C-terminal fusions FMO03130 (Lost), FMO06869 (Polo), FMO07294 (Imp), FMO11010 (Yp3), FMO12286 (Jar). Plasmids for expressing tagged proteins in S2 cells were generated by cloning coding sequences into pEntr/SD (Thermofisher, K242020), and recombining the coding sequences into pAc5 promoter destination vectors (pAWM and pAWF). Site directed mutagenesis was performed as described above to generate Bsd.Q545* and Polo.T182A. To generate GST-Bsd for *E. coli* expression, the *bsd* coding sequence was subcloned into pGex4T-1 (Sal1/NotI). The Vrk3 mammalian expression construct was generated by recombining pDONR223-VRK3 [Addgene 23687, [67]] into pDEST-CMV-3xFLAG-EGFP [Addgene 122845, [68]]; pRcCMV-Myc-Plk1 was used without modification [Addgene 41160, [69]].

Immunohistochemistry and *in situ* hybridization

Antibodies used were α-Mef2 (1:1000, gift from R. Cripps), α-Tropomyosin (1:600, Abcam, MAC141), α-PLK1-phospho-T210 (1:100, Abcam, ab39068), α-GFP (1:600, Torrey Pines Biolabs, TP-401), α-GFP (1:300, Aves Labs, GFP-1020), α-dsRed (1:300, Takara, 632392), α-γ-tubulin (1:300, Sigma, T5326), and α-βgal (1:100, Promega, Z3781). Embryo antibody staining was performed as described [24]; HRP-conjugated secondary antibodies in conjunction with the TSA system (Molecular Probes) were used to detect primary antibodies. For S2 cell labeling, cells ($5x10^6$) were transfected per manufacturer's specifications (Lipofectamine 3000, Invitrogen; applies to all transfections in this study), cultured at 25°C in Schneider's Drosophila medium (Sigma, S9895) supplemented with 10% heat-inactivated fetal bovine serum (FBS, Invitrogen, 10082147) for 72h, collected and washed once with S2 medium. Cells were then seeded into a 6-well-plate with a glass cover slip and incubated for 1h. The cells were washed twice with PBS and fixed with 4% PFA for 15min, and then washed 3 times with PBS. After 1h blocking in 25%NGS/PBST, cells were incubated with α-FLAG antibody (1:1000,

Sigma, F3165) and α-Myc antibody (1:1000, Sigma, PLA001) in PBST containing 0.5% BSA at 4°C for 12h. After five PBS washes, cells were mounted in Vectashield with DAPI (H-1000).

We performed in situ hybridization as previously described (Williams et al., 2015), except Dig-labeled probes were detected with HRP-conjugated α-Dig (Roche, 11207733910, 1:500) in conjunction with the TSA system (Molecular Probes). Probe templates were generated by cloning PCR products from DNA LD16949 and LD39409 into PCR2.1 vector. Templates were validated by Sanger sequencing.

Imaging and image quantification

Embryos were imaged with a Zeiss LSM800 confocal microscope; cells were imaged by confocal or with an inverted Zeiss AxioObserver. For time-lapse imaging, dechorionated St12 embryos were mounted in halocarbon oil and scanned at 6min intervals. For single-frame live imaging, embryos were dechorionated, mounted in PBT, and directly scanned. Control and mutant embryos were prepared and imaged in parallel where possible, and imaging parameters were maintained between genotypes. Fluorescent intensity and cell morphology measurements were made with ImageJ software.

Phenotypic scoring, analysis, and visualization

Each embryonic hemisegment has 30 distinct muscles with a fixed pattern as shown in Fig. 1B. Muscle phenotypes were analyzed in hemisegments A2-A7, in a minimum of nine embryos per genotype. For global muscle analyses, a Tropomyosin antibody was used to visualize all 30 muscles. For individual muscle analyses, GFP was expressed under the control of a muscle-restricted Gal4 driver to visualize a subset of muscles. For both assays, muscles were assigned a phenotype: normal, missing, elongation defect, attachment site defect. A '% Defective' was calculated for each of the 30 muscles in minimum of 54 hemisegments. '% Defective = # of abnormal muscles/hemisegments scored. % Defective was then converted to a schematic heat map on the embryonic muscle pattern. 'Histologic Score' was calculated using the following scale: missing=3, elongation defect=2, attachment site defect=1, normal=0. Histologic Score = sum of phenotypic score/number of embryos analyzed as described [70]. Myoblast fusion was quantified by counting the number of lacZ+ myonuclei per hemisegment in *rP298.nlacZ* embryos. Fusion Index = #lacZ nuclei experimental/#lacZ nuclei control.

GST pull down and Mass spectrometry

GST-Bsd and GST was purified from *E.coli* by standard methods and stored at -80°C in 1ml aliquots. 12-24hr embryo lysates were collected by homogenizing dechorionated embryos in a Dounce homogenizer with 100 μl of lysis buffer (60mM Tris pH7.5, 80mM NaCl, 6mM EDTA pH8.0, 2% Triton X-100, 5mM 1-Naphthyl potassium phosphate, 2mM PMSF, 1X Sigma

Phosphatase Inhibitor II, 1X Protease Inhibitor) per 10μl of embryos. The lysate was then centrifuged at 15,000 RCF for 10min to pellet large debris. The supernatant was diluted to a final protein concentration of 1mg/μl, aliquoted in 100μl volumes, and flash frozen. For affinity purification, 500μl of dialyzed GST-Bsd or GST was bound to 50μl of PBS washed glutathione sepharose beads (GE Healthcare, 17-0756-01) and incubated at 4°C for 30min. The beads were washed with PBS-1% Triton X-100. Embryo lysates (100mg protein/ml) were incubated with the protein-bound beads at 4°C for 4hr; the beads were then washed three times and submitted to the Washington University Proteomics Core Lab for liquid chromatography-mass spectrometry (1260 Infinity II Bio-Inert LC System, Agilent Technologies).

***In vitro* Bsd kinase assay**

For cell free *in vitro* kinase assay, GST-Bsd and GST-Polo were purified from *E.coli* as described above. GST-Bsd were incubated with GST-Polo for 30 min at 30°C in 20 mM HEPES(pH 7.5), 2 mM $MgCl_2$, 1 mM DTT, and 0.5 mM ATP. Reactions were stopped by the addition of 5x SDS loading buffer. Samples were separated by SDS-PAGE and blotted with α-PLK1-phospho-T210 (1:500, Abcam, ab39068) and α-GST (1:1000, Cell signaling technology, #2625).

Immunoprecipitation and Western blotting

For *Drosophila* proteins, S2 cells ($8x10^6$) were transfected with 2μg of each plasmid in 6-well plates. Cells were cultured for 48h, incubated with 2mM $CuSO_4$ for 24h (for FMO plasmids only), collected, washed twice with PBS, lysed with 600μl IP buffer (20 mM Hepes, pH=7.4, 150 nM NaCl, 1% NP40, 1.5 mM $MgCl_2$, 2 mM EGTA, 10 mM NaF, 1 mM Na_3VO_4, 1X proteinase inhibitor), incubated on ice for 30 min, centrifuged at 12000Xg for 15min. The supernatant was collected, incubated with 2μl α-FLAG (Sigma, F3165) or α-Myc (PLA001, Sigma) overnight at 4°C, and then incubated with 30μl Dynabeads (Invitrogen, 10007D) for 4hr at 4°C. The beads were washed 5X with IP buffer, and immunoblotted with α-Myc (1:3000) or α-FLAG (1:2000).

For *in vitro* phosphorylation assays, immunoprecipitation was carried out as described, except that anti-Phosphothreonine antibody (1:125, Abcam, ab9337) was used for immunoblotting. For *in vivo* phosphorylation assays, 200 *Polo-GFP* and 200 *bsd*[1]; *Polo-GFP* embryos were homogenized in 600μl IP buffer, large debris was removed by 15min centrifugation (12,000Xg), and immunoprecipitation was carried out as described above using 2μl α-GFP (Torrey Pines Biolabs, TP-401).

For mammalian proteins, HEK293T cells were seeded in 6-well plates, grown to 60% confluency at 37°C and 5%CO_2 in Dulbecco's modified Eagle's medium (DMEM; Invitrogen)

supplemented with 10% heat-inactivated FBS. Cells were transfected with 2μg of each plasmid and cultured for 48h. Immunoprecipitations were carried out as described above. Plk1 phosphorylation was directly assayed without immunoprecipitation using α-PLK1-phospho-T210 (1:500, Abcam, ab39068).

Western blots were performed by standard method using precast gels (#456-1096, BioRad), and imaged with the ChemiDoc XRS+ system (BioRad).

siRNA knockdown and inhibitor treatments

For siRNAs, C2C12 cells were seeded in 6-well-plate and grown in standard conditions to 60% confluency in growth medium (10% FBS in DMEM), and transfected 10 nM duplexed 27nt siRNAs (Integrated DNA Technologies). Transfection efficiency was monitored with Cy3 transfection controls (Trifecta Kit, Integrated DNA Technologies). After 24hr, the growth media was changed to differentiation media (2% horse serum in DMEM). After 7 days differentiation, cells were fixed for 15min in 4% PFA and stained with α-alpha-actinin antibody (A7811, Sigma, 1:1000).

For Volasertib, C2C12 cells were seeded in 6-well-plate and grown in standard conditions to nearly 100% confluency in growth medium, and treated with 100nM Volasertib or DMSO for 24h in growth medium (No.S2235, Selleck chem). Then the growth medium was changed to differentiation medium (2% horse serum in DMEM), with 100nM Volasertib or DMSO and incubated for 48h. Cells were incubated in differentiation medium without Volasertib or DMSO for additional 5 days, fixed and stained as described above.

Quantitative real time PCR

Total RNA was extracted with RNeasy mini kit (74104, Qiagen), and quantified (Nanodrop 2000). The cDNA was prepared by reverse transcription with M-MLV Reverse Transcriptase (28025013, Thermo) with 2000ng RNA. PowerUp Sybr Green Master Mix (A25742, Thermo) and ABI StepOne system (Applied Biosystems) were used for quantitative RT-PCR. Quantification was normalized to *GAPDH* or *RpL32*. Primers used were:

Vrk1-F-5`-ACAGGTTTATGATAATGGACCGC-3`

Vrk1-R-5`-CTGGTCAGGGTTCTTGTGACT-3`

Vrk2-F-5`-CCGCACATGGACACTCTGTA-3`

Vrk2-R-5`-CTTGCTGGATGAACTCCCAG-3`

Vrk3-F-5`-ATCAAGGACCCAGAAGTGGAGA-3`

Vrk3-R-5`-TTCTTCCATTTGTTCACTTGCAGA-3`

Gapdh-F-5`-TGTAGACCATGTAGTTGAGGTCA-3`

Gapdh-R-5`-AGGTCGGTGTGAACGGATTTG-3`

Bsd- F-5`-TCAACGCTAAGCACTCCGTT-3`

Bsd-R-5`-CGCCTCTGCTCCATGTCTAG-3`

Rp32- F-5`-ATGCTAAGCTGTCGCACAAATG-3`

Rp32- R-5`-GTTCGATCCGATACCGATGT-3`

Bioinformatic and statistical analysis

Protein alignments were generated in ClustalX, and phylogenetic analyses were performed with DNAMAN (Lynnon Corporation) using the observed divergency distance method. ATPbind was used to predict Bsd ATP binding residues; informatics predictions were compared to the VRK1 ATP binding pocket described in [33].

Statistical analyses were performed with GraphPad Prism 8 software, and significance was determined with the unpaired, one-tailed student's t-test or Mann-Whitney test (for non-Gaussain distributions). Gaussian distribution fit curve and skew distribution fit curve were generated with Origin 2019 software. Sample sizes are indicated in the figure legends. Data collection and data analysis were routinely performed by different authors to prevent potential bias. All individuals were included in data analysis.

Data Availability

The data that support all experimental findings of this study are available. Raw data necessary to reproduce all statistical analyses and results in the paper are provided in the Source Data File provided with this paper, or from A.N.J. upon request.

References

1. Glover, D.M., I.M. Hagan, and A.A. Tavares. (1998) Polo-like kinases: a team that plays throughout mitosis. *Genes Dev*, **12**(24): p. 3777-87.
2. Joukov, V. and A. De Nicolo. (2018) Aurora-PLK1 cascades as key signaling modules in the regulation of mitosis. *Sci Signal*, **11**(543).
3. Pintard, L. and V. Archambault. (2018) A unified view of spatio-temporal control of mitotic entry: Polo kinase as the key. *Open Biology*, **8**(8): p. 180114.
4. Kachaner, D., et al. (2014) Interdomain allosteric regulation of Polo kinase by Aurora B and Map205 is required for cytokinesis. *J Cell Biol*, **207**(2): p. 201-11.
5. Ebrahimi, S., H. Fraval, M. Murray, R. Saint, and S.L. Gregory. (2010) Polo kinase interacts with RacGAP50C and is required to localize the cytokinesis initiation complex. *Journal of Biological Chemistry*, **285**(37): p. 28667-28673.
6. Carmena, M., et al. (2012) The chromosomal passenger complex activates polo kinase at centromeres. *PLoS Biology*, **10**(1): p. e1001250.
7. Morgan, D.O. (1995) Principles of CDK regulation. *Nature*, **374**(6518): p. 131-4.
8. Tateno, M., Y. Nishida, and T. Adachi-Yamada. (2000) Regulation of JNK by Src during Drosophila development. *Science*, **287**(5451): p. 324-7.
9. Johnson, G.L. and R. Lapadat. (2002) Mitogen-activated protein kinase pathways mediated by ERK, JNK, and p38 protein kinases. *Science*, **298**(5600): p. 1911-2.
10. Saxton, R.A. and D.M. Sabatini. (2017) mTOR Signaling in Growth, Metabolism, and Disease. *Cell*, **169**(2): p. 361-371.
11. Hiratsuka, T., I. Bordeu, F.M. Watt, and G. Pruessner. (2020) Regulation of ERK basal and pulsatile activity control proliferation and exit from the stem cell compartment in mammalian epidermis. **117**(30): p. 17796-17807.
12. Lénárt, P., et al. (2007) The Small-Molecule Inhibitor BI 2536 Reveals Novel Insights into Mitotic Roles of Polo-like Kinase 1. *Current Biology*, **17**(4): p. 304-315.
13. Liu, D., O. Davydenko, and M.A. Lampson. (2012) Polo-like kinase-1 regulates kinetochore–microtubule dynamics and spindle checkpoint silencing. *Journal of Cell Biology*, **198**(4): p. 491-499.
14. Cabral, G., T. Laos, J. Dumont, and A. Dammermann. (2019) Differential Requirements for Centrioles in Mitotic Centrosome Growth and Maintenance. *Dev Cell*, **50**(3): p. 355-366.e6.
15. Lane, H.A. and E.A. Nigg. (1996) Antibody microinjection reveals an essential role for human polo-like kinase 1 (Plk1) in the functional maturation of mitotic centrosomes. *J Cell Biol*, **135**(6 Pt 2): p. 1701-13.
16. Liu, X. and R.L. Erikson. (2002) Activation of Cdc2/cyclin B and inhibition of centrosome amplification in cells depleted of Plk1 by siRNA. *Proc Natl Acad Sci U S A*, **99**(13): p. 8672-6.
17. Archambault, V. and D.M. Glover. (2009) Polo-like kinases: conservation and divergence in their functions and regulation. *Nat Rev Mol Cell Biol*, **10**(4): p. 265-75.
18. Archambault, V., P.P. D'Avino, M.J. Deery, K.S. Lilley, and D.M. Glover. (2008) Sequestration of Polo kinase to microtubules by phosphopriming-independent binding to Map205 is relieved by phosphorylation at a CDK site in mitosis. *Genes Dev*, **22**(19): p. 2707-20.
19. Bonner, A.M., S.E. Hughes, and R.S. Hawley. (2020) Regulation of Polo Kinase by Matrimony Is Required for Cohesin Maintenance during Drosophila melanogaster Female Meiosis. *Current Biology*, **30**(4): p. 715-722.e3.
20. Kachaner, D., D. Garrido, H. Mehsen, K. Normandin, H. Lavoie, and V. Archambault. (2017) Coupling of Polo kinase activation to nuclear localization by a bifunctional NLS is required during mitotic entry. *Nature communications*, **8**(1): p. 1701.
21. McCormick, L.E. and S.L. Gupton. (2020) Mechanistic advances in axon pathfinding. *Curr Opin Cell Biol*, **63**: p. 11-19.
22. Schnorrer, F. and B.J. Dickson. (2004) Muscle building; mechanisms of myotube guidance and attachment site selection. *Dev Cell*, **7**(1): p. 9-20.
23. Yang, S., A. Weske, Y. Du, J.M. Valera, K.L. Jones, and A.N. Johnson. (2020) FGF signaling directs myotube guidance by regulating Rac activity. *Development*, **147**(3).

24. Johnson, A.N., M.H. Mokalled, J.M. Valera, K.D. Poss, and E.N. Olson. (2013) Post-transcriptional regulation of myotube elongation and myogenesis by Hoi Polloi. *Development*, **140**(17): p. 3645-56.
25. Bothe, I. and M.K. Baylies. (2016) Drosophila myogenesis. *Curr Biol*, **26**(17): p. R786-91.
26. Williams, J., N.G. Boin, J.M. Valera, and A.N. Johnson. (2015) Noncanonical roles for Tropomyosin during myogenesis. *Development*, **142**(19): p. 3440-52.
27. Guerin, C.M. and S.G. Kramer. (2009) RacGAP50C directs perinuclear gamma-tubulin localization to organize the uniform microtubule array required for Drosophila myotube extension. *Development*, **136**(9): p. 1411-21.
28. Schnorrer, F., I. Kalchhauser, and B.J. Dickson. (2007) The transmembrane protein Kon-tiki couples to Dgrip to mediate myotube targeting in Drosophila. *Dev Cell*, **12**(5): p. 751-66.
29. Chen, E.H., B.A. Pryce, J.A. Tzeng, G.A. Gonzalez, and E.N. Olson. (2003) Control of myoblast fusion by a guanine nucleotide exchange factor, loner, and its effector ARF6. *Cell*, **114**(6): p. 751-762.
30. Kramer, S.G., T. Kidd, J.H. Simpson, and C.S. Goodman. (2001) Switching repulsion to attraction: changing responses to slit during transition in mesoderm migration. *Science*, **292**(5517): p. 737-40.
31. Katzemich, A., R.J. West, A. Fukuzawa, S.T. Sweeney, M. Gautel, J. Sparrow, and B. Bullard. (2015) Binding partners of the kinase domains in Drosophila obscurin and their effect on the structure of the flight muscle. *J Cell Sci*, **128**(18): p. 3386-97.
32. Martín-Doncel, E. and A.M. Rojas. (2019) VRK1 functional insufficiency due to alterations in protein stability or kinase activity of human VRK1 pathogenic variants implicated in neuromotor syndromes. **9**(1): p. 13381.
33. Shin, J., et al. (2011) NMR solution structure of human vaccinia-related kinase 1 (VRK1) reveals the C-terminal tail essential for its structural stability and autocatalytic activity. *J Biol Chem*, **286**(25): p. 22131-8.
34. Sunkel, C.E. and D.M. Glover. (1988) polo, a mitotic mutant of Drosophila displaying abnormal spindle poles. *J Cell Sci*, **89 (Pt 1)**: p. 25-38.
35. Deák, P.t., M. Donaldson, and D.M. Glover. (2003) Mutations in mákos, a Drosophila gene encoding the Cdc27 subunit of the anaphase promoting complex, enhance centrosomal defects in polo and are suppressed by mutations in twins/aar, which encodes a regulatory subunit of PP2A. *Journal of Cell Science*, **116**(20): p. 4147-4158.
36. Bate, M., *The mesoderm and its derivatives*, in *The Development of Drosophila melanogaster*, M. Bate, Editor. 1993, CSHLP: Cold Spring Harbor, NY. p. pp1013-1090.
37. Seki, A., J.A. Coppinger, C.Y. Jang, J.R. Yates, and G. Fang. (2008) Bora and the kinase Aurora a cooperatively activate the kinase Plk1 and control mitotic entry. *Science*, **320**(5883): p. 1655-8.
38. Willems, E., M. Dedobbeleer, M. Digregorio, A. Lombard, P.N. Lumapat, and B. Rogister. (2018) The functional diversity of Aurora kinases: a comprehensive review. *Cell Division*, **13**(1): p. 7.
39. Zhu, Q., et al. (2019) Viral-Mediated AURKB Cleavage Promotes Cell Segregation and Tumorigenesis. *Cell Rep*, **26**(13): p. 3657-3671.e5.
40. Gregory, S.L., S. Ebrahimi, J. Milverton, W.M. Jones, A. Bejsovec, and R. Saint. (2008) Cell division requires a direct link between microtubule-bound RacGAP and Anillin in the contractile ring. *Current Biology*, **18**(1): p. 25-29.
41. D'Avino, P.P., M.S. Savoian, L. Capalbo, and D.M. Glover. (2006) RacGAP50C is sufficient to signal cleavage furrow formation during cytokinesis. *Journal of Cell Science*, **119**(Pt 21): p. 4402-4408.
42. Somers, W.G. and R. Saint. (2003) A RhoGEF and Rho family GTPase-activating protein complex links the contractile ring to cortical microtubules at the onset of cytokinesis. *Developmental Cell*, **4**(1): p. 29-39.
43. Tillery, M.M.L., C. Blake-Hedges, Y. Zheng, R.A. Buchwalter, and T.L. Megraw, *Centrosomal and Non-Centrosomal Microtubule-Organizing Centers (MTOCs) in Drosophila melanogaster*. 2018. p. E121.
44. Blau, H.M., C.P. Chiu, and C. Webster. (1983) Cytoplasmic activation of human nuclear genes in stable heterocaryons. *Cell*, **32**(4): p. 1171-80.

45. Mathieu, J., et al. (2013) Aurora B and Cyclin B Have Opposite Effects on the Timing of Cytokinesis Abscission in Drosophila Germ Cells and in Vertebrate Somatic Cells. *Developmental Cell*, **26**(3): p. 250-265.
46. Li, Y., O. Barbash, and J.A. Diehl, *11 - Regulation of the Cell Cycle*, in *The Molecular Basis of Cancer (Fourth Edition)*, J. Mendelsohn, et al., Editors. 2015, W.B. Saunders: Philadelphia. p. 165-178.e2.
47. Ou, T., G. Huang, B. Wilson, P. Gontarz, J.B. Skeath, and A.N. Johnson. (2021) A genetic screen for regulators of muscle morphogenesis in Drosophila. *G3 (Bethesda)*.
48. Cullen, C.F., A.L. Brittle, T. Ito, and H. Ohkura. (2005) The conserved kinase NHK-1 is essential for mitotic progression and unifying acentrosomal meiotic spindles in Drosophila melanogaster. *J Cell Biol*, **171**(4): p. 593-602.
49. van Roosmalen, W., et al. (2015) Tumor cell migration screen identifies SRPK1 as breast cancer metastasis determinant. *J Clin Invest*, **125**(4): p. 1648-64.
50. Han, X., et al. (2017) Knockdown of Serine-Arginine Protein Kinase 1 Inhibits the Growth and Migration in Renal Cell Carcinoma Cells. *Oncol Res*, **25**(3): p. 389-395.
51. Liu, H., X. Hu, Y. Zhu, G. Jiang, and S. Chen. (2016) Up-regulation of SRPK1 in non-small cell lung cancer promotes the growth and migration of cancer cells. *Tumour Biol*, **37**(6): p. 7287-93.
52. Nakagawa, O., et al. (2005) Centronuclear myopathy in mice lacking a novel muscle-specific protein kinase transcriptionally regulated by MEF2. *Genes Dev*, **19**(17): p. 2066-77.
53. Bustos, F., et al. (2020) Functional Diversification of SRSF Protein Kinase to Control Ubiquitin-Dependent Neurodevelopmental Signaling. *Dev Cell*, **55**(5): p. 629-647.e7.
54. Beaven, R., N.S. Dzhindzhev, Y. Qu, I. Hahn, F. Dajas-Bailador, H. Ohkura, and A. Prokop. (2015) Drosophila CLIP-190 and mammalian CLIP-170 display reduced microtubule plus end association in the nervous system. *Molecular Biology of the Cell*, **26**(8): p. 1491-1508.
55. Geisbrecht, E.R. and D.J. Montell. (2002) Myosin VI is required for E-cadherin-mediated border cell migration. *Nature Cell Biology*, **4**(8): p. 616-620.
56. Yoong, L.-F., H.-K. Lim, H. Tran, S. Lackner, Z. Zheng, P. Hong, and A.W. Moore. (2020) Atypical Myosin Tunes Dendrite Arbor Subdivision. *Neuron*, **106**(3): p. 452-467.e8.
57. Glover, D.M. (2005) Polo kinase and progression through M phase in Drosophila: a perspective from the spindle poles. *Oncogene*, **24**(2): p. 230-7.
58. Adams, R.R., A.A. Tavares, A. Salzberg, H.J. Bellen, and D.M. Glover. (1998) pavarotti encodes a kinesin-like protein required to organize the central spindle and contractile ring for cytokinesis. *Genes Dev*, **12**(10): p. 1483-94.
59. Carmena, M., M.G. Riparbelli, G. Minestrini, A.M. Tavares, R. Adams, G. Callaini, and D.M. Glover. (1998) Drosophila polo kinase is required for cytokinesis. *J Cell Biol*, **143**(3): p. 659-71.
60. Goldstein, A.Y., Y.N. Jan, and L. Luo. (2005) Function and regulation of Tumbleweed (RacGAP50C) in neuroblast proliferation and neuronal morphogenesis. *Proc Natl Acad Sci U S A*, **102**(10): p. 3834-9.
61. Scheeff, E.D., J. Eswaran, G. Bunkoczi, S. Knapp, and G. Manning. (2009) Structure of the pseudokinase VRK3 reveals a degraded catalytic site, a highly conserved kinase fold, and a putative regulatory binding site. *Structure*, **17**(1): p. 128-38.
62. Park, C.H., H.G. Ryu, S.H. Kim, D. Lee, H. Song, and K.T. Kim. (2015) Presumed pseudokinase VRK3 functions as a BAF kinase. *Biochim Biophys Acta*, **1853**(7): p. 1738-48.
63. Jia, Z., et al. (2019) A requirement of Polo-like kinase 1 in murine embryonic myogenesis and adult muscle regeneration. **8**.
64. Nose, A., T. Isshiki, and M. Takeichi. (1998) Regional specification of muscle progenitors in Drosophila: the role of the msh homeobox gene. *Development*, **125**(2): p. 215-23.
65. Ranganayakulu, G., D.A. Elliott, R.P. Harvey, and E.N. Olson. (1998) Divergent roles for NK-2 class homeobox genes in cardiogenesis in flies and mice. *Development*, **125**(16): p. 3037-3048.
66. Hadwiger, G., S. Dour, S. Arur, P. Fox, and M.L. Nonet. (2010) A monoclonal antibody toolkit for C. elegans. *PLoS One*, **5**(4): p. e10161.
67. Johannessen, C.M., et al. (2010) COT drives resistance to RAF inhibition through MAP kinase pathway reactivation. *Nature*, **468**(7326): p. 968-72.
68. Agrotis, A. and N. Pengo. (2019) Redundancy of human ATG4 protease isoforms in autophagy and LC3/GABARAP processing revealed in cells. **15**(6): p. 976-997.

69. Golsteyn, R.M., S.J. Schultz, J. Bartek, A. Ziemiecki, T. Ried, and E.A. Nigg. (1994) Cell cycle analysis and chromosomal localization of human Plk1, a putative homologue of the mitotic kinases Drosophila polo and Saccharomyces cerevisiae Cdc5. *J Cell Sci*, **107 (Pt 6)**: p. 1509-17.
70. He, X., et al. (2017) Bap180/Baf180 is required to maintain homeostasis of intestinal innate immune response in Drosophila and mice. *Nature Microbiology*, **2**(6): p. 17056.

Acknowledgements

We thank Helen McNeill and Mayssa Mokalled for critical reading of the manuscript, Jean-Rene Huynh and the *Drosophila* community for stocks and reagents, and our reviewers for great comments to improve the manuscript. Our LC-MS was performed by the Washington University Proteomics Core. ANJ was supported by NIH R01AR070299. PHT was supported by NIH R01MH067122.

Author Contributions

Conceptualization: A.N.J., S.Y.; Methodology: A.N.J.; Formal analysis: S.Y., J.MA., Y.D., J.T., P.H., A.N.J.; Investigation: S.Y., J.MA., Y.D., J.T., P.H., A.N.J.; Resources: P.H., A.N.J.; Data curation: S.Y., Y.D., A.N.J.; Writing original draft: A.N.J.; Visualization: S.Y., A.N.J.; Supervision: S.Y., A.N.J.; Project administration: A.N.J.; Funding acquisition: A.N.J.

Figure Legends

Figure 1. The ser/thr kinase Bsd regulates muscle morphogenesis. (A) Myogenic phenotype in *bsd*^{1} mutants. Stage 16 embryos labeled with Tropomyosin. Doral Transverse 1 (DT1) and Longitudinal Oblique (LO1) muscles are pseudocolored orange and green. Control (w^{1118}) embryos showed a stereotypic pattern of body wall muscles. *bsd*^{1} embryos showed severe defects in muscle morphology, including rounded and bent muscles. The *bsd*^{1} myogenic defects were completely rescued in embryos harboring the *bsd*-containing genomic construct CH321-61F090. Outcrossing CH321-61F090 restored the *bsd*^{1} myogenic phenotype. (B) Quantification of muscle phenotypes. Muscles were scored in hemisegments A2-A7 of St16 embryos. Muscles with abnormal phenotypes (missing muscles, muscles with attachment site defects, and muscles that failed to elongate) were scored "defective". The frequencies of muscle defects are shown as a heat map on the stereotypic muscle pattern in one embryonic hemisegment, as previously reported [23]. (n) number of hemisegments scored in a minimum of 9 embryos. See Fig. S1E for statistical analysis. (C) Genetic mapping details and Bsd protein domains. Two overlapping deficiencies failed to complement *bsd*^{1} (dashed lines indicate breakpoints outside the genomic region shown; see Fig. S1 for transheterozygous phenotypes). The Bsd protein has one kinase domain (KD; orange) that is conserved among the VRK protein family; the Bsd KD is divided by a unique linker (green). The position of a conserved ATP binding pocket is also shown (purple). (D-E) Analysis of individual muscles lineages in *bsd*^{1} embryos. *5053>GFP* (D) and *slou>GFP* (E) are expressed in non-overlapping founder cell populations and highlight specific muscle morphologies. Stage 16 embryos labeled for GFP (green) and Tropomyosin (violet). *bsd*^{1} Ventral Lateral 1 (VL1) muscles made incorrect or incomplete tendon attachments (D, white arrowheads) and were often rounded (not shown). *bsd*^{1} DT1, LO1, and Ventral Transverse 1 (VT1) muscles also made incorrect tendon attachments (E, white arrowheads; see Movie 1) or remained round (blue arrowhead). (F) Histogram of VL1, DT1, LO1, and VT1 phenotypes from *5053>GFP* and *slou>GFP* embryos (n≥60 hemisegments per muscle per genotype). (G) Histologic scores for muscles analyzed in (F). Open circles (wild-type), closed circles (*bsd*^{1}). (H) Fusion index in St12 embryos shows myoblast fusion was modestly reduced in *bsd*^{1} embryos. Each data point represents one hemisegment (n≥60 per genotype). See Materials and Methods for statistical parameters. Significance determined by Fisher's exact test (B,F), and unpaired student's t-test (H). **($p<0.01$), ****($p<0.0001$). Error bars represent SEM.

Figure 2. Bsd expression in the mesoderm is progressively enriched during muscle development. (A) *w^{1118}* embryos immunolabeled for Bsd (green) and Mef2 (violet). Bsd was detected in Mef2+ muscle cells throughout myogenesis. Bsd protein levels in the mesoderm peaked at during Stage 12. Bsd also appeared to be enriched in myonuclei (see Fig. S2E,F). (B) Bsd kinase activity in the mesoderm directs muscle morphogenesis. Control (*w^{1118}*), *bsd^1/Df(2R)BSC199 UAS.Bsd*, *bsd^1/Df(2R)BSC199 24B.Gal4>Bsd,* and *bsd^1/Df(2R)BSC199 24B.Gal4>Bsd.I129A* embryos labeled for Tropomyosin. DT1, LO1, and VL1 muscles are pseudocolored orange, green, and violet. *bsd^1* embryos that expressed wild-type Bsd in the mesoderm showed improved muscle morphology; *bsd^1* embryos that expressed catalytically inactive Bsd.I129A showed extensive muscle defects. (C) Quantitative real time PCR analysis of *bsd* mRNA showed equivalent expression between transgenic lines. (D) Quantification of muscle phenotypes as described in Fig. 1B. (E) Space filling model of Bsd. The predicted ATP binding pocket is colored with Iso129 shaded violet. Significance was determined by one-way ANOVA (C) and Fisher's exact test (D). *($p<0.05$), **($p<0.01$), ****($p<0.0001$). Error bars represent SEM.

Figure 3. Bsd and Polo kinase act in a common myogenic pathway. (A) Relative abundance of Bsd interacting proteins recovered from 12-24hr embryo lysates, determined by MS. See Table S2 for detailed quantification. (B,C) Immunoprecipitation of S2 cell lysates transfected with Bsd, Bsd.Q545*, and Polo. Full length Bsd interacted with Polo in reciprocal experiments, but Bsd.Q545* and Polo did not interact. (D) *$polo^1$* VL1 muscle phenotype. Stage 16 embryos labeled for *5053>GFP* (green) and Tropomyosin (violet). *$polo^1$* VL1 muscles were rounded (blue arrowhead) and made incorrect or incomplete tendon attachments (white arrowheads). (E) *$polo^1$* DT1, LO1, and VT1 muscle phenotypes. Stage 16 embryos labeled for *slou>GFP* (green) and Tropomyosin (violet). *$polo^1$* LO1 muscles had attachment site defects (white arrowheads). (F) Muscle phenotypes in *bsd^1 $polo^1$* double mutants. Stage 16 embryos labeled with Tropomyosin. DT1, LO1, and VL1 muscles are pseudocolored orange, green, and violet. The frequency and severity of muscle morphology defects was comparable between *bsd^1* and *bsd^1 $polo^1$* embryos. Quantification of muscle phenotypes is as described in Fig. 1B (see Fig. S3G for statistical analysis). (G) DT1, LO1, and VT1 phenotypes in *bsd^1 $polo^1$* double mutant embryos (labeled as in E). The frequency and severity of DT1, LO1, and VT1 phenotypes was comparable between *bsd^1* and *bsd^1 $polo^1$* embryos. (H) Histogram of VL1, DT1, LO1, and VT1 phenotypes from *5053>GFP* and *slou>GFP* embryos ($n\geq60$ hemisegments per muscle per genotype). Significance was determined by Fisher's exact test. (ns) not significant.

Figure 4. Bsd activates Polo to direct myotube guidance. (A) Polo immunoprecipitated from S2 cell lysates and blotted with anti-phosphothreonine (pThr). Cells transfected with Bsd showed significantly more phosphorylated Polo than controls. (B) Bsd.Myc, Polo.Flag, and Polo.T182A.Flag were transfected into S2 cells; transgenic proteins were detected with anti-Myc (red, Bsd) and anti-Flag (green, Polo). Polo localized to the nucleus in a subset of control cells (left column). The frequency of cells showing nuclear Polo localization was increased in cells co-transfected with Bsd (second column from left). Inactivatable Polo (T182A) did not localize to the nucleus in control cells (third column from left) or in cells co-transfected with Bsd (right column). (C) Dot plot showing percent of cells with nuclear Polo per microscope field from (B). (D) Endogenous GFP-tagged Polo was immunoprecipitated from embryo lysates and blotted with pThr. *bsd*^{1} embryo lysates showed significantly less phosphorylated Polo than controls. (E) Stage 12 embryos immunolabeled for Polo phosphorylated at Thr182 (Polo^{pT182}, green) and Mef2 (violet). Polo^{pT182} levels were reduced in the myonuclei of *bsd*^{1} embryos compared to controls. (F) Polo^{pT182} fluorescent intensity from embryos shown in (4D and S4F). Polo^{pT182} fluorescence intensity is dynamic during Stage 12, and significantly increased in control (*bsd*^{1}*/Cyo*) embryos. Polo^{pT182} fluorescence intensity did not increase in Stage 12 *bsd*^{1} embryos. Control and experimental embryos were derived from the same preparation. (G) Activated Polo rescues the *bsd* phenotype. *bsd*^{1} *UAS.Polo*^{T182D} and *bsd*^{1} *Mef2.Gal4>Polo*^{T182D} embryos labeled for Tropomyosin. DT1, LO1, and VL1 muscles are pseudocolored orange, green, and violet. *bsd*^{1} embryos that expressed active (phosphomimetic) Polo.T182D in the mesoderm showed improved muscle morphology compared to *bsd*^{1} embryos. Note that expressing Polo.T182D in otherwise wild-type embryos caused a modest muscle phenotype, which may explain the incomplete rescue of the *bsd*^{1} phenotype. Quantification of myogenic phenotypes is as described in Fig. 1B. (12E) Stage 12 early, (12L) Stage 12 late. Significance was determined by unpaired student's t-test (A,D,E), one-way AONVA (C), and Fisher's Exact Test (G). (ns) not significant. **($p<0.01$), ****($p<0.0001$). Error bars represent SEM.

Figure 5. Aurora kinases are inactive in the post-mitotic mesoderm. (A) Stage 10 and Stage 12 embryos labeled for *aurA* (left, green), *aurB* (middle, green) or pH3 (right, green) and Mef2 (violet). *aurA*, *aurB* and pH3 are expressed in mesoderm of Stage 10 embryos, but are excluded from the somatic mesoderm in Stage 12 embryos. (B) Nascent myotubes that expressed *rp298>eGFP* were sorted to enrich for myogenic RNA, and RNAseq results were reported in [23]. (C) Analysis of *aurA*, *aurB* and *bsd* mRNA expression in nascent myotubes

from the experiment shown in (B). (D) Stage 12 embryos immunolabeled for activated Polo ($Polo^{pT182}$, green) and Mef2 (violet). $Polo^{pT182}$ levels were comparable between *aurA*, *aurB*, and control embryos. Control and experimental embryos were derived from the same preparations. (E) The Fly-FUCCI system. A tissue-specific Gal4 activates fluorescent fusion proteins that are post-transcriptionally controlled to identify cell cycle phases *in vivo*. (F) Stage 11 embryos that expressed Fly-FUCCI transgenes under the control of *Mef2.Gal4*, immunolabeled for GFP-$E2F1_{1-230}$ (green) and RFP-$CycB_{1-266}$ (violet). Embryos that expressed *aurB* in the mesoderm showed more cells in G2/M (white arrowheads) than G1 (blue arrowheads) or S (orange arrowheads). Percent of dividing cells in G2/M phase (GFP/RFP double positive cells) are plotted; each data point represents a single hemisegment. (n≥12 hemisegments, from 6 embryos). Significance was determined by one-way ANOVA (C) and unpaired student's t test (D,F). (ns) not significant. ***($p<0.001$), ****($p<0.0001$). Error bars represent SEM.

Figure 6. Bsd directs microtubule reorganization during myotube guidance. (A) tum^{DH15} VL1, DT1, LO1, and VT1 muscle phenotypes. Stage 16 embryos labeled for *5053>GFP* (green) or *slou>GFP* (green) and Tropomyosin (violet). Tum regulates microtubule reorganization during myogenesis [27], and tum^{DH15} muscles showed attachment site defects similar to bsd^1 muscles. (B) Histogram of VL1, DT1, LO1, and VT1 phenotypes from *5053>GFP* and *slou>GFP* embryos (n≥60 hemisegments per muscle per genotype). (C) Live imaging frames showing LO1 myotubes in Stage 12-15 embryos that expressed the microtubule minus end binding protein Nod.GFP (green) and the F-actin binding fluorophore LifeAct.RFP (violet). Transgene expression was controlled by *slou.Gal4*. Live imaging initiated once Nod.GFP fluorescence was detectable (0min). Control LO1 myotubes showed a linear array of microtubule minus ends at the onset of imaging (white arrowheads). Nod.GFP did not co-localize with F-actin at the myotube leading edges, indicative of microtubules with a minus-ends-in conformation. The linear configuration of microtubule minus ends in bsd^1 LO1 myotubes was delayed; Nod.GFP remained cortical through the early stages of myotube elongation (blue arrowheads). bsd^1 microtubule minus ends often overlapped with the F-actin domain (red arrowhead). See Fig. S6D for F-actin heatmap. (D) Quantification of Nod.GFP distribution. GFP fluorescence was traced in each frame of three independent live-imaging experiments per genotype. Nod.GFP localization was stable in control myotubes, with a low roundness score (more linear), and an angle consistent with the final LO1 attachment angle. bsd^1 myotubes showed fluctuating Nod.GFP localization, with an overall high roundness score (more cortical) and an angle that deviates from the control attachment angle. (E) Single confocal scans of multinucleate LO1

myotubes from Stage 12 *slou>GFP* embryos labeled for γ-tubulin (green), GFP (violet), and DAPI (blue). Control (*bsd*^{1}*/Cyo*) myotubes showed both cortical and internal cytoplasmic γ-tubulin foci, with internal foci concentrated toward the myotube leading edges (red arrowheads). *bsd*^{1} myotubes had significantly fewer internal γ-tubulin foci compared to controls, but an equivalent number of cortical γ-tubulin foci. (F) Quantification of γ-tubulin foci in multinucleate Stage 12 myotubes. See Fig. S6E,F for γ-tubulin foci in mononucleate founder cells. Embryos in (E,F) were derived from the same preparation. Significance was determined by Fisher's exact test (B), Wilcoxon signed-rank test (D) and unpaired student's t-test (F). (ns) not significant. **($p<0.01$), ****($p<0.0001$). Error bars represent SEM.

Figure 7. The Bsd orthologue Vrk3 is required for myotube elongation. (A) C2C12 cells treated with siRNAs against murine Vrk3 or with an inhibitor of Plk1 (Volasterib, 100nM). Cells were fixed after 7 days in differentiation media, and labeled for α-actinin (green) to detect differentiated myotubes. Vrk3 knockdown and Volasterib treated myotubes were shorter than controls and were often rounded. (B) Myotube length distribution. Solid lines show the Gaussian distribution fit curve (blue) and skew distribution fit curve (red). Vrk3 RNAi and Volasterib treated myotubes were shorter than controls (C) Quantification of cumulative myotube length. (D) Myotube roundness scores. Vrk3 RNAi and Volasterib treated myotubes showed a higher roundness score, indicating increased circularity. (E) Immunoprecipitation of HEK293 cell lysates showed a physical interaction between Vrk3 and Plk1. (F) Western blot of HEK293 cell lysates transfected with Vrk3 and Plk1. Vrk3 promoted Plk1 phosphorylation at Thr210. (G) Control (*w*^{1118}), *bsd*^{1} *UAS.VRK3*, and *bsd*^{1} *24B.Gal4>VRK3* embryos labeled for Tropomyosin. DT1, LO1, and VL1 muscles are pseudocolored orange, green, and violet. *bsd*^{1} embryos that expressed human VRK3 in the mesoderm showed improved muscle morphology (H) Model showing Polo activation transitions from AurB in mitotic tissues to Bsd in post-mitotic tissues. Polo controls cytoskeletal regulatory module to direct cytokinesis and myotube guidance. Significance was determined by unpaired student's t-test (B, D) and Mann–Whitney u-test (C). **($p<0.01$), ****($p<0.0001$). Error bars represent SEM.

Movie Captions

Movie 1. Bsd regulates myotube guidance. Live imaging of LO1 myotubes from Stage 12 *slou>eGFP,nRFP* embryos. *bsd*^{1} myotubes failed to elongate anteriorly and attached at the posterior of the segment. GFP (green), RFP (violet). Arrowheads denote the myotube dorsal leading edge.

Movie 2. Bsd does not regulate tendon cell number or position. Live imaging of tendon cells from Stage 12 *sr>eGFP* embryos. Tendon cells in *bsd*^{1} embryos were indistinguishable from wild-type embryos.

Movie 3. Tum regulates myotube guidance. Live imaging of an LO1 myotubes from Stage 12 *tum*^{DH15} *slou>eGFP* embryos. *tum*^{DH15} myotubes often elongated toward the incorrect muscle attachment site.

Movie 4. Microtubule reorganization is delayed in *bsd*^{1} myotubes. Live imaging of LO1 myotubes from Stage 12 *slou>Nod.GFP,LifeAct.RFP* embryos. Nod.GFP localizes to microtubule minus-ends; LifeAct localizes to F-actin. The formation of linear minus-end arrays was delayed in *bsd*^{1} myotubes. GFP (green), RFP (violet).

Figure 1. The ser/thr kinase Bsd regulates muscle morphogenesis

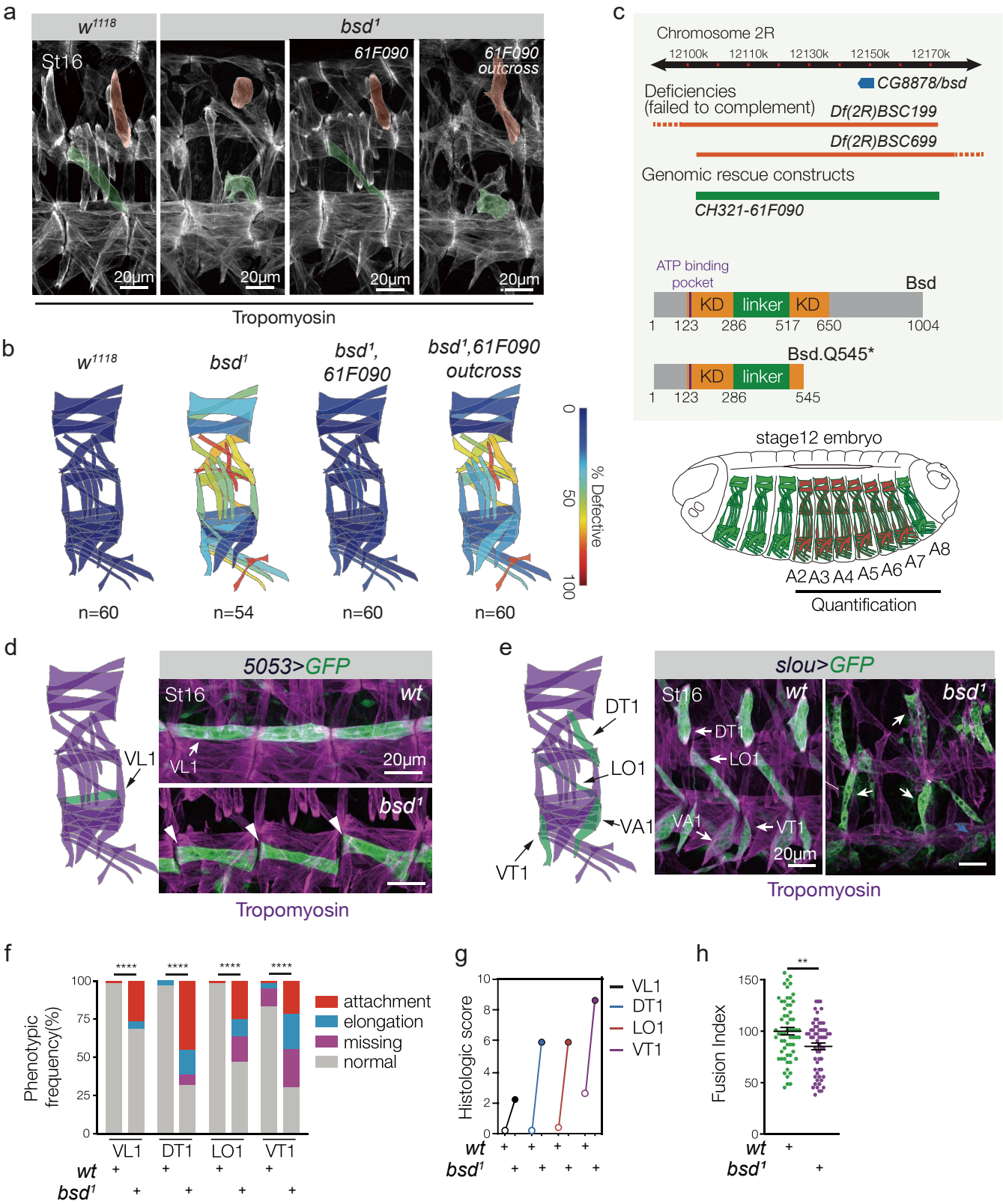

Figure 2. Bsd expression in the mesoderm is progressively enriched during muscle development

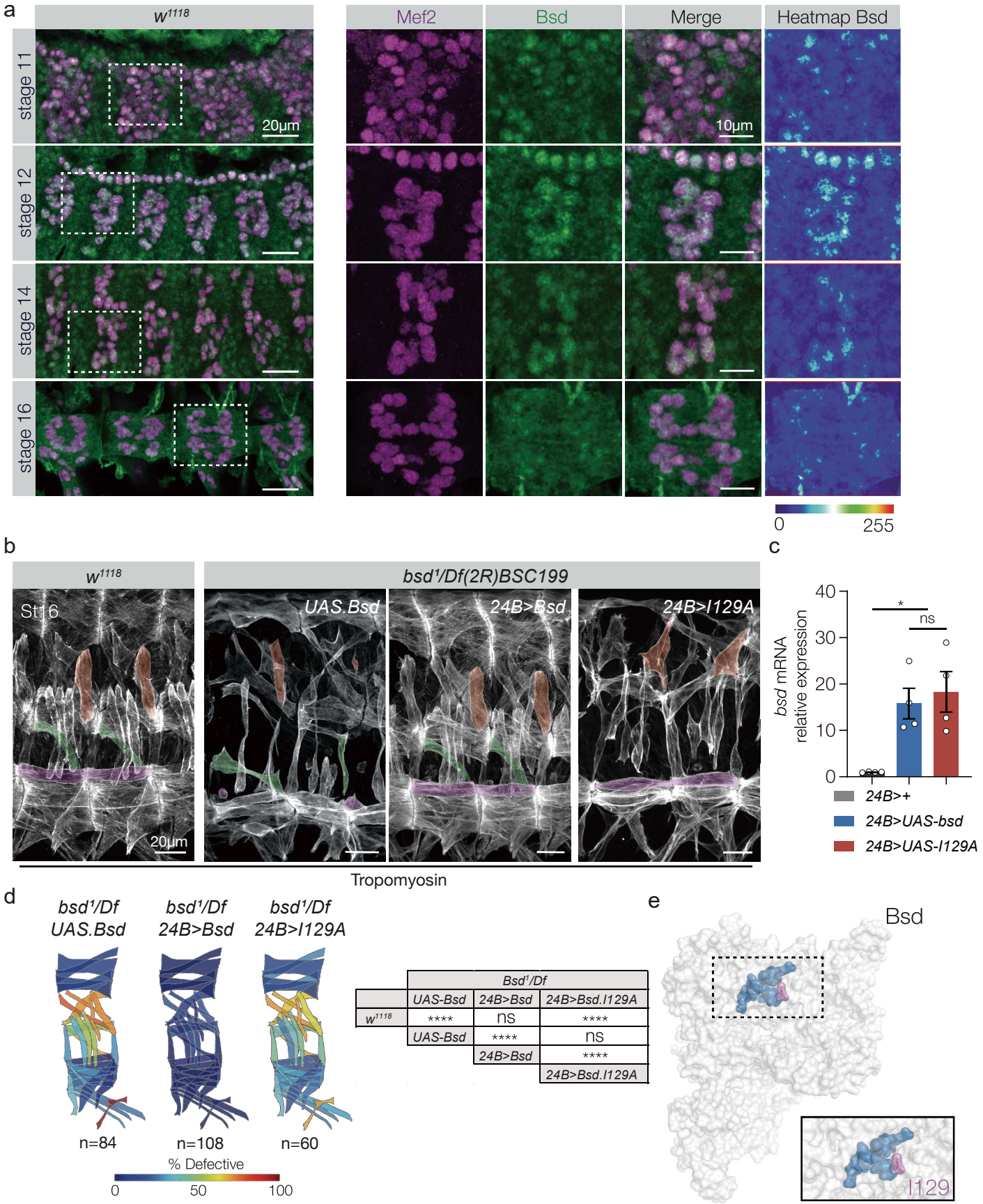

Figure 3. Bsd and Polo kinase act in a common myogenic pathway

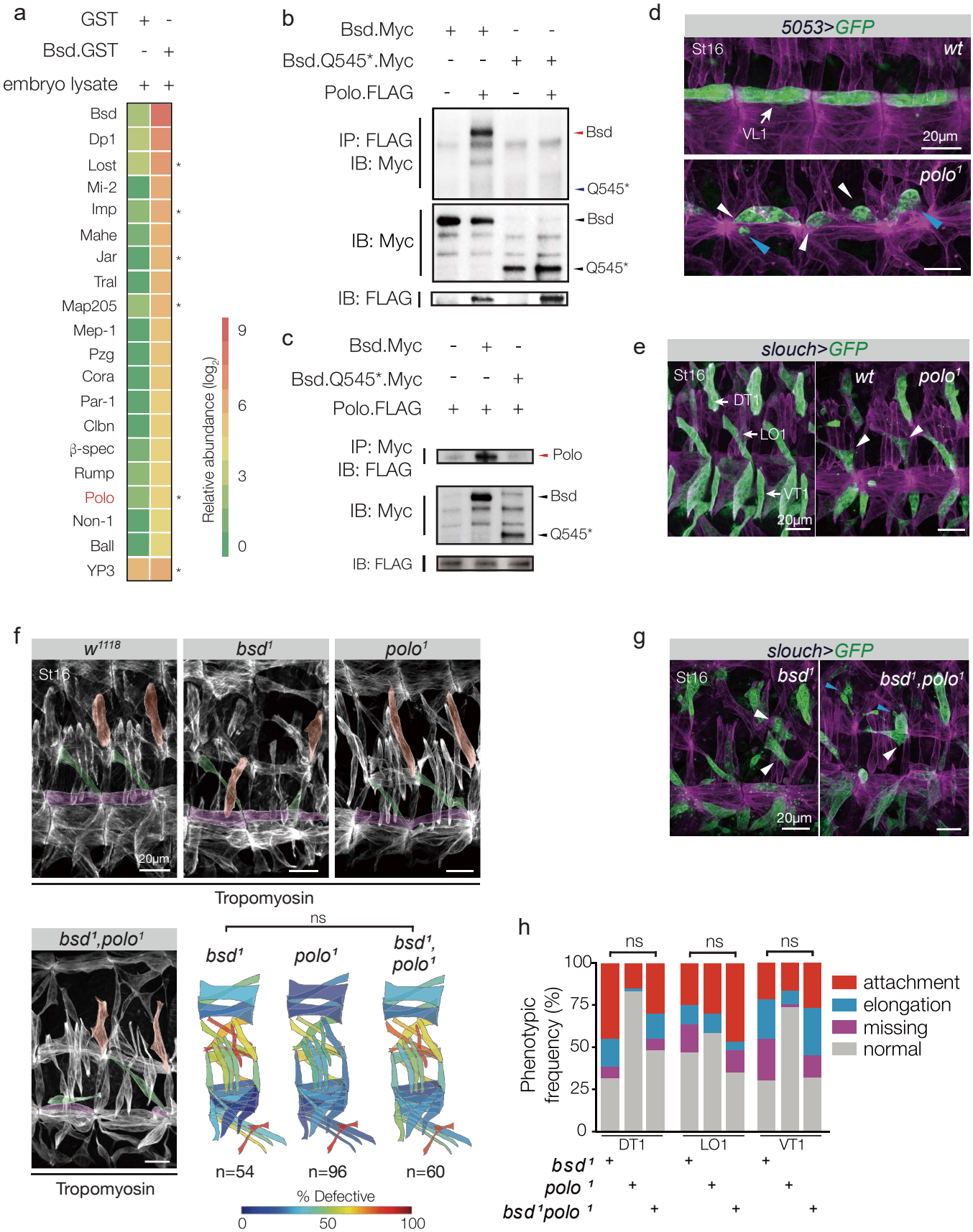

Figure 4. Bsd activates Polo to direct myotube guidance

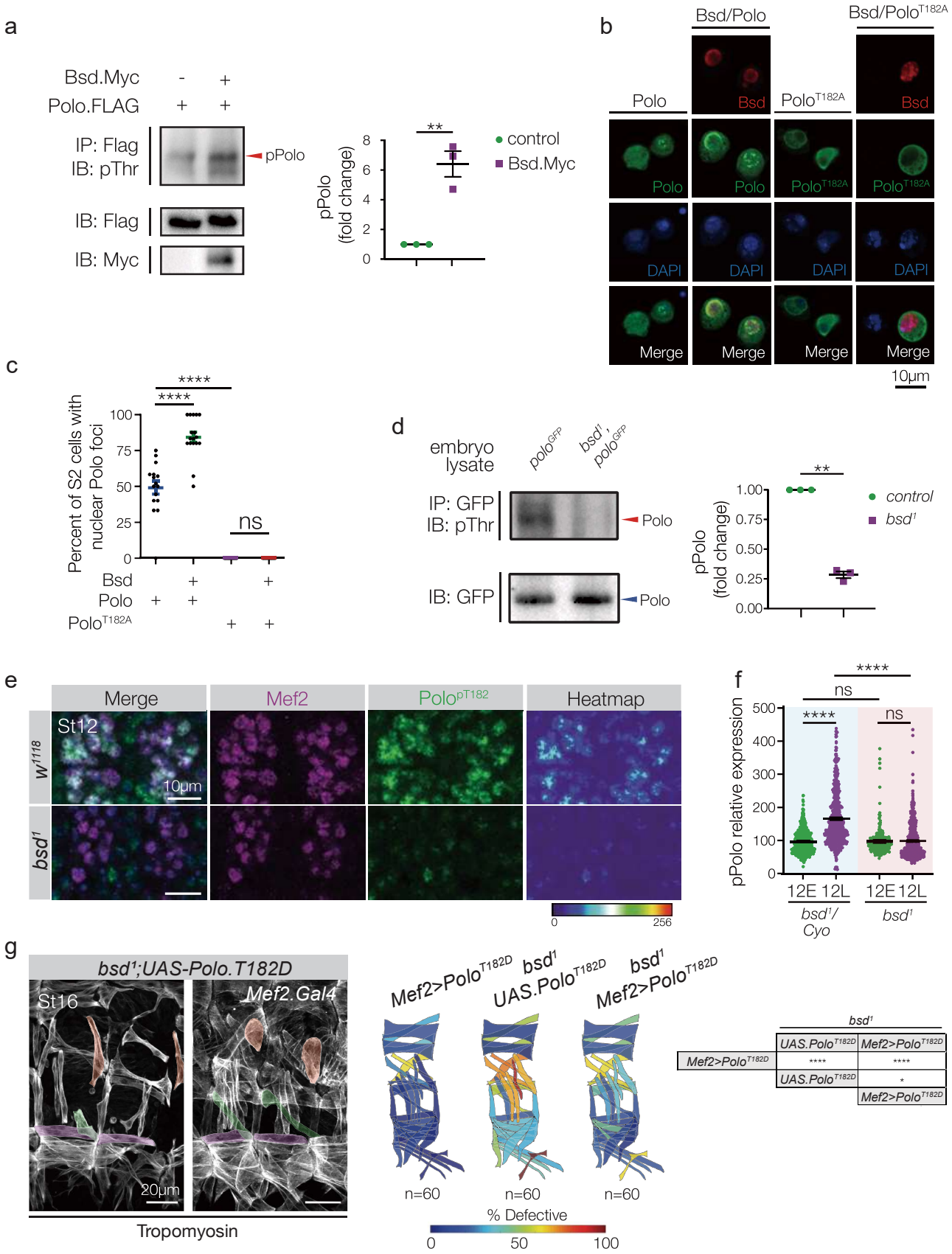

Figure 5 AurA and AurB are not active in the post-mitotic mesoderm

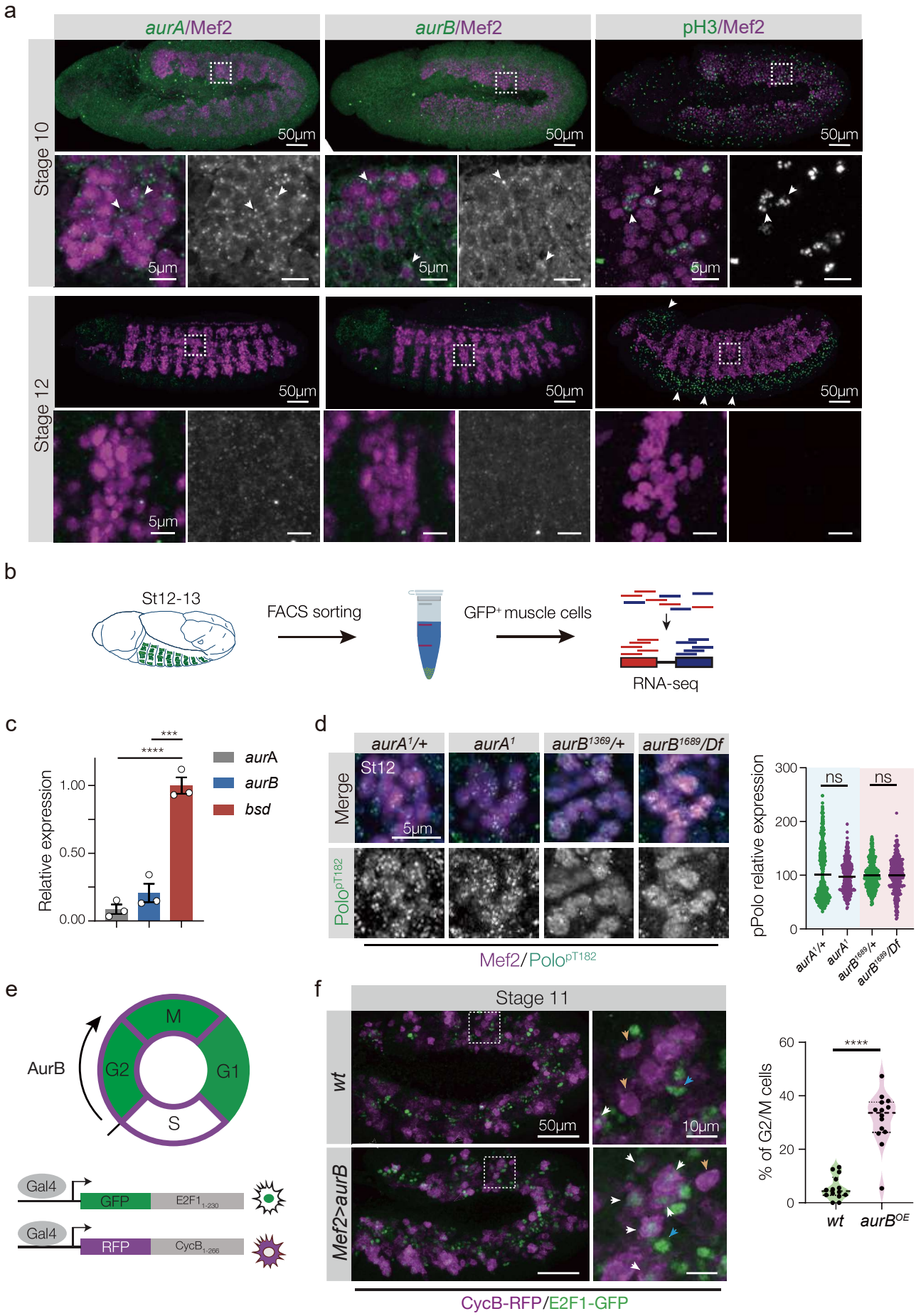

Figure 6. Bsd directs microtubule reorganization during myotube guidance

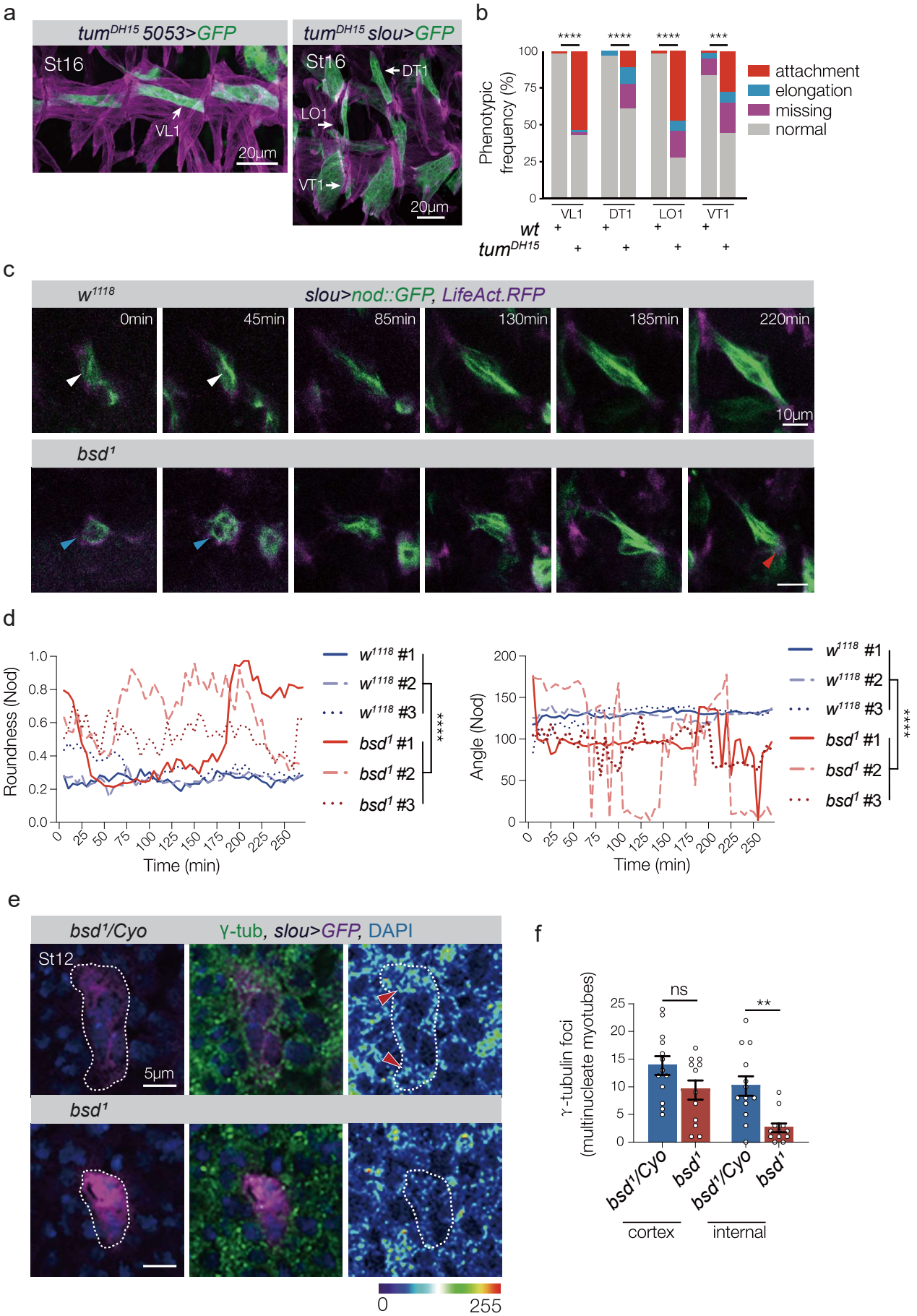

Figure 7. The Bsd orthologue Vrk3 is required for myotube elongation

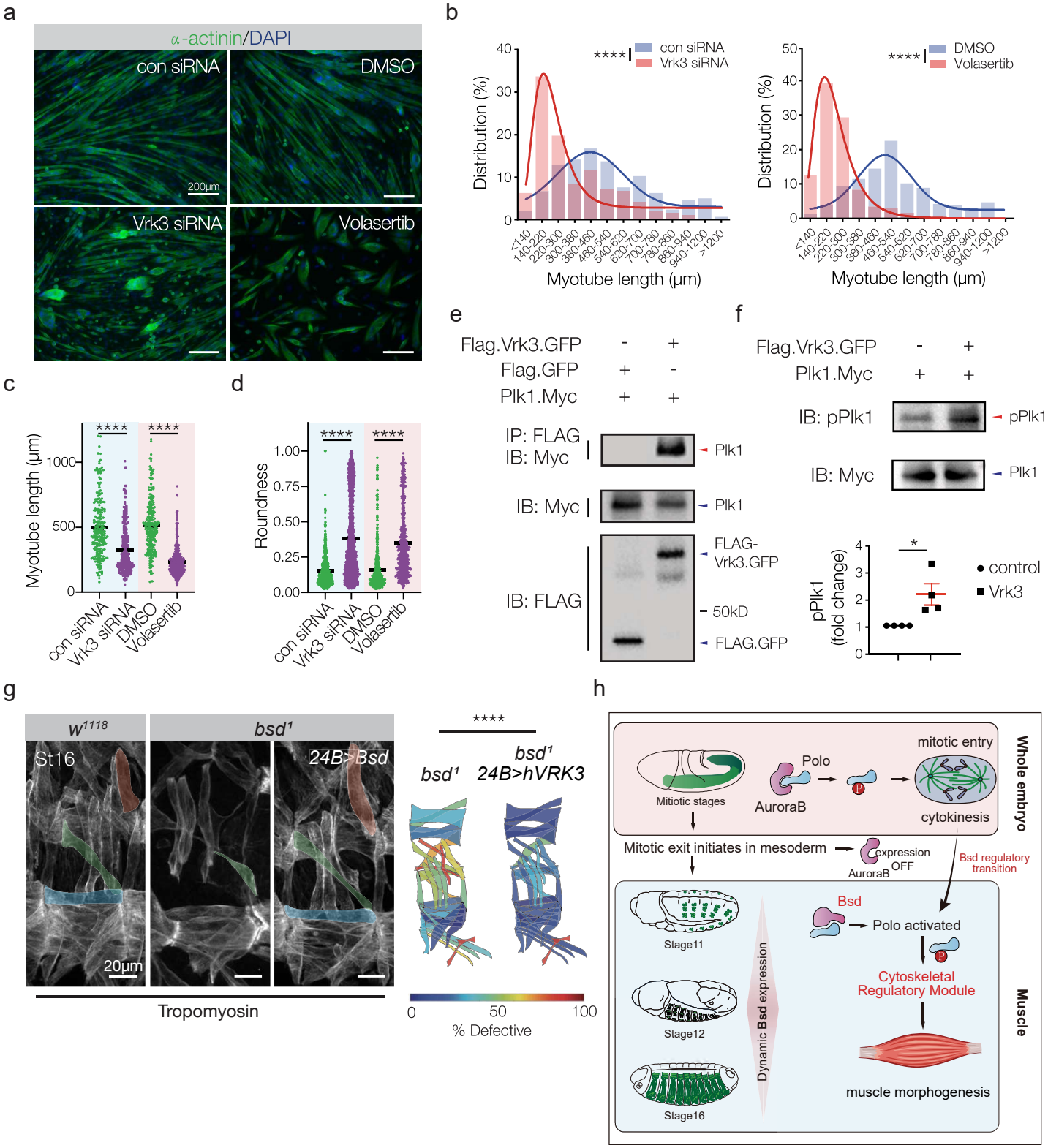

Supplementary Information

Spatiotemporal expression of regulatory kinases directs the transition from mitosis to cellular morphogenesis

Shuo Yang[1], Jennifer McAdow[1], Yingqiu Du[1], Jennifer Trigg[2], Paul H. Taghert[2], and Aaron N. Johnson[1,3]

[1]Department of Developmental Biology
[2]Department of Neuroscience
Washington University School of Medicine
St. Louis, MO 63110

[3]Author for correspondence: anjohnson@wustl.edu
Running Title: Bsd activates Polo during myogenesis

Supplementary Table Titles

Table S1. Embryonic expression patterns of *Drosophila* and zebrafish protein kinases.

Table S2. Mass spectrometry results, related to Figure 3A.

Table S3. Source information for reagents.

`

Figure S1, related to Figure 1

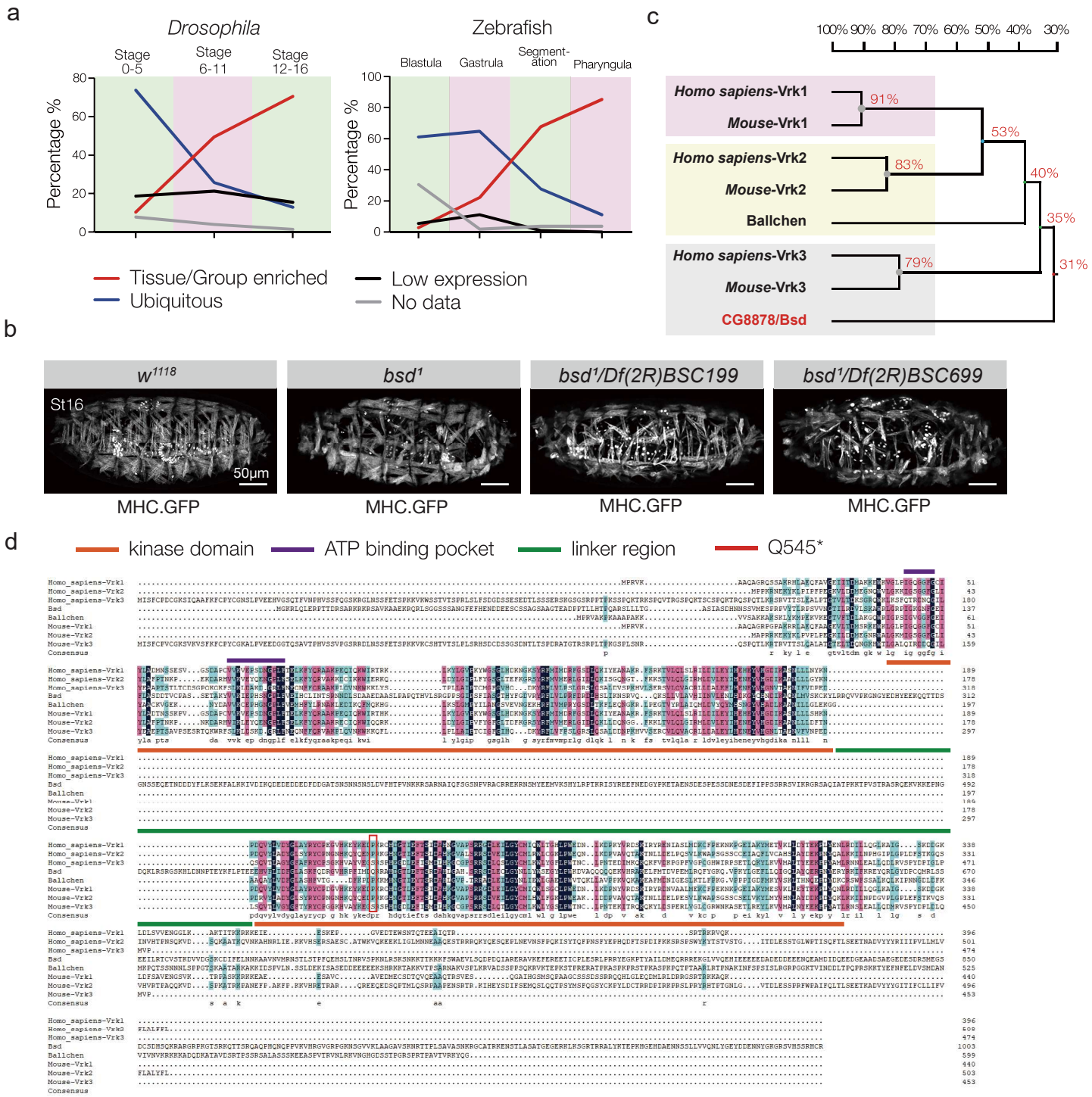

	Bsd[1]		
	-	61F090	61F090 outcross
w^{1118}	****	ns	****
	-	****	ns
		61F090	****
			61F090 outcross

Supplementary Figures

Figure S1, related to Figure 1. (A) *in silico* expression analysis of *Drosophila* and zebrafish protein kinases. Embryonic expression patterns for all kinases were queried in Flybase and Zfin, and those with reported expression patterns were graphed. Expression patterns were subdivided by embryonic stage (Stages 0-5 in *Drosophila* occur prior to gastrulation), and classified as Tissue/Group Enriched, (meaning the kinase was expressed in a single tissue or a group of tissues but not all tissues), Ubiquitous, or Low Expression (in which the expression pattern was too faint to categorize). No Data indicates the expression pattern is known for only a subset of embryonic stages. See Table S1 for individual expression patterns. (B) *bsd* deficiency mapping. Live Stage 16 embryos that expressed Myosin Heavy Chain (MHC)-GFP. bsd^1/*Df(2R)BSC199* and bsd^1/*Df(2R)BSC699* embryos phenocopied bsd^1 embryos. A control (w^{1118}) embryo is shown for comparison. (C) Phylogenetic analysis of human, mouse, and fly Vrk proteins. The homology tree was generated using observed divergency as the distance method. The percent homology among species is shown. (D) Protein alignment of the Vrk proteins from (C); black shading shows identical residues in all species, pink shading shows residues that are the same in most species, blue shading shows residues that are the same in at least 50% of species. The position of the bsd^1 Q545* mutation is given (red box). Residues in the previously defined Kinase Domain (orange line) and ATP binding pocket (violet) for human Vrk1 are shown. Note that the Bsd kinase domain is split by a unique linker region (green line), and the C-termini of the Vrk proteins show low sequence homology. (E) Fisher's exact test of the myogenic phenotypes shown in Fig. 1B. Significance indicates pairwise comparison between two genotypes. (F) Stage 12 *5053>GFP* and *slou>GFP* embryos labeled for GFP. Control and bsd^1 embryos showed an equivalent number of GFP+ founder cells. Significance was determined by unpaired student's t-test. (ns) not significant. ****($p<0.0001$).Error bars represent SEM.

Figure S2, related to Figure 2

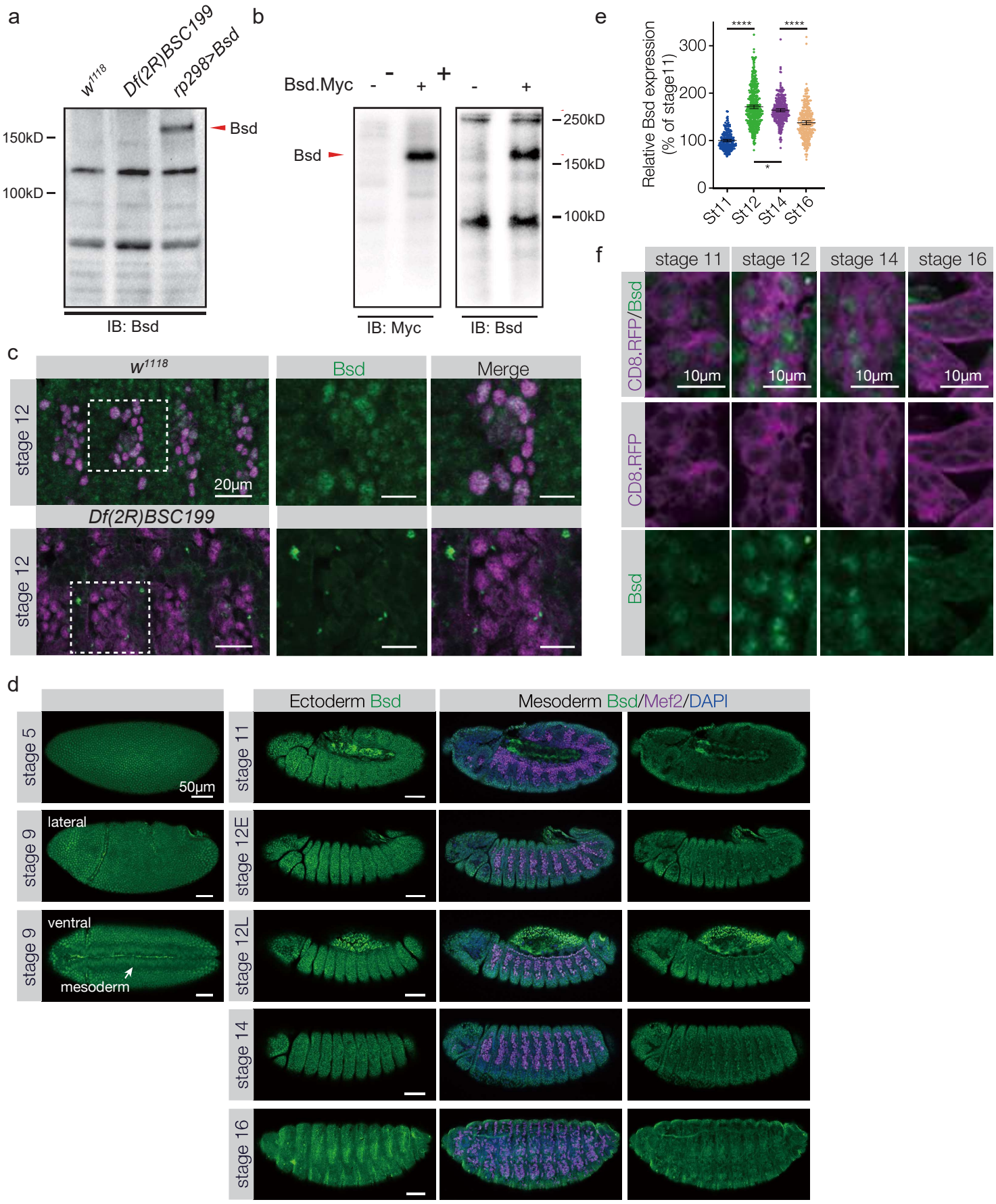

Figure S2, related to Figure 2. (A-C) Validation of a Bsd antibody. (A) Western blots of control (w^{1118}), *Df(2R)BSC199,* and *rp298>Bsd* embryo lysates using the Bsd antibody. UAS/Gal4 expressed Bsd was detectable, but we could not detect endogenous Bsd by Western blot. (B) Western blot of S2 cell lysates transfected with control or Bsd.Myc expressing plasmids. The Bsd and Myc antibodies recognized proteins of the same molecular weight. (C) Stage 12 embryos immunolabeled with the Bsd antibody (green) and Mef2 (violet). Signal from the Bsd antibody was not observed in *Df(2R)BSC199* body wall muscle precursors. The embryos shown were prepared in parallel. (D) Complete embryonic expression of Bsd. Embryos were immunolabeled as in (C). Multiple confocal projections are shown for each embryo to compare expression in the ectoderm and the mesoderm. Bsd was ubiquitously expressed prior to gastrulation (Stage 5), and Bsd expression remained high in the ectoderm after gastrulation. Bsd expression in the mesoderm increased from Stage 11 to Stage 12, and then decreased. (E) Relative Bsd expression in the mesoderm, normalized to Stage 11. (F) Embryos immunolabeled with the Bsd antibody (green) and membrane localized *Mef2>CD8.RFP* (violet). Bsd localization was enriched in the nucleus of Mef2+ cells through Stage 14. Significance was determined by one-way ANOVA. *($p<0.05$), ****($p<0.0001$). Error bars represent SEM.

Figure S3, related to Figure 3

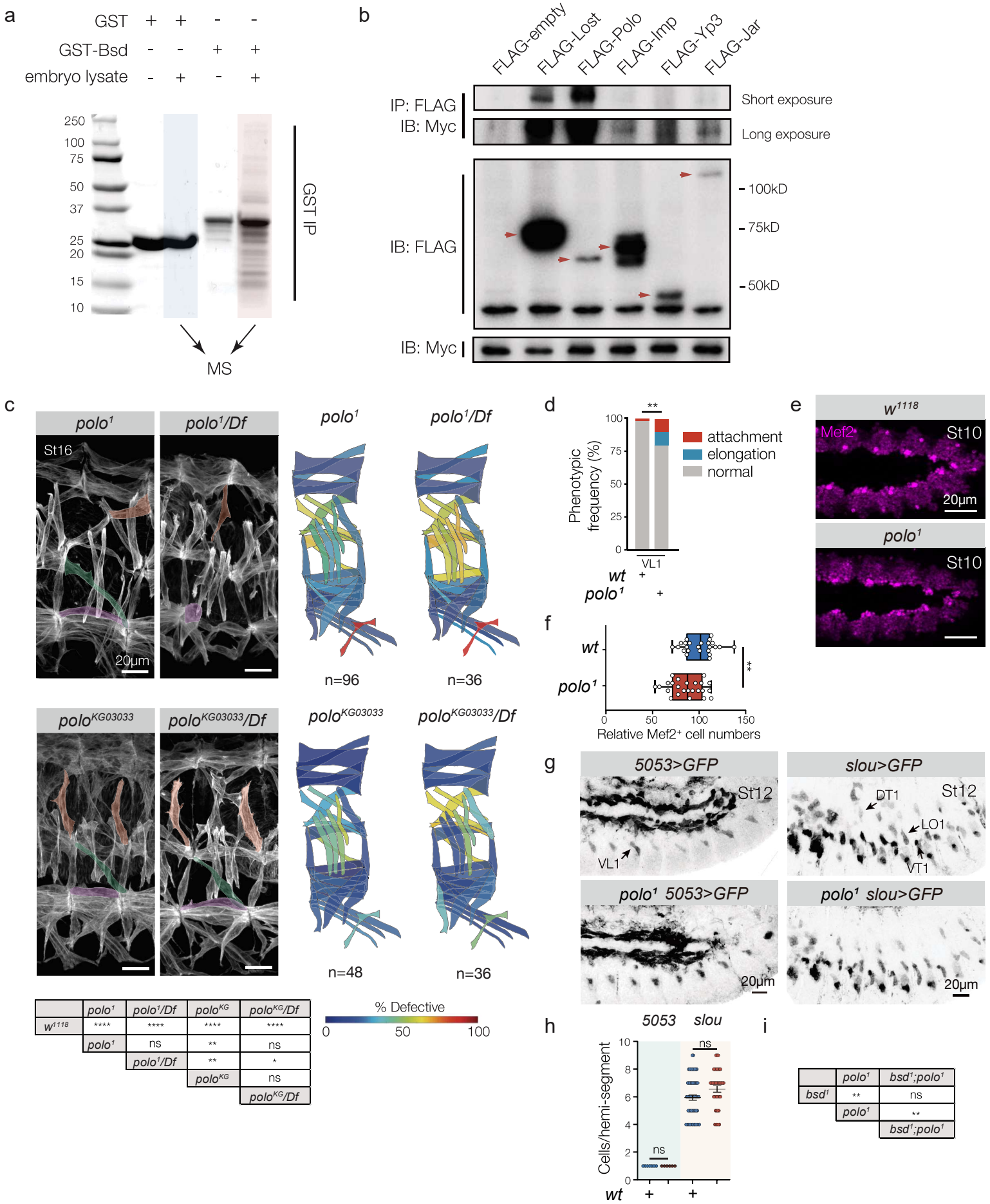

	polo1	polo1/Df	poloKG	poloKG/Df
w1118	****	****	****	****
polo1		ns	**	ns
polo1/Df			**	*
poloKG				ns
poloKG/Df				

	polo1	bsd1;polo1
bsd1	**	ns
polo1		**
bsd1;polo1		

Figure S3, related to Figure 3. (A) Coomassie stained control gel for the GST-based precipitation experiment described in (Fig. 3A). Bsd-bound GST beads (lane 5; red shading) recovered a large number of unique bands compared to control GST beads (lane 3; blue shading). (B) Immunoprecipitation of S2 cell lysates transfected with Bsd and candidate proteins identified by MS. Bsd interacted with all five proteins, but Polo showed the strongest interaction. (C) Myogenic phenotypes in *polo* mutants. Stage 16 embryos labeled with Tropomyosin. DT1, LO1, and VL1 muscles are pseudocolored orange, green, and violet. The *polo* alleles showed stronger phenotypes in trans to *Df(3L)BSC447*, as expected for hypomorphic alleles. Heat maps and Fisher's exact test of the myogenic phenotypes are as described in Figs. 1B and S1E. (D) Histogram of $polo^{1}$ VL1 phenotypes (n=54). Significance was determined by Fisher's exact test. (E) Stage 10 control embryos and $polo^{1}$ embryos labeled for Mef2. (F) Statistical analysis of embryos shown in (E). Each data point represents the number of Mef2+ cells in a single hemisegment; $polo^{1}$ embryos had 14.2% fewer Mef2+ cells than controls. (G) Stage 12 *5053>GFP* embryos and *slou>GFP* embryos labeled for GFP. Control and $polo^{1}$ embryos showed an equivalent number of GFP+ cells. (H) Statistical analysis of embryos shown in (G). Significance was determined by student's t-test. (I) Fisher's exact test of the myogenic phenotypes shown in Fig. 3F. (ns) not significant, *($p<0.05$), **($p<0.01$), ***($p<0.001$), ****($p<0.0001$). Error bars represent SEM.

Figure S4, related to Figure 4

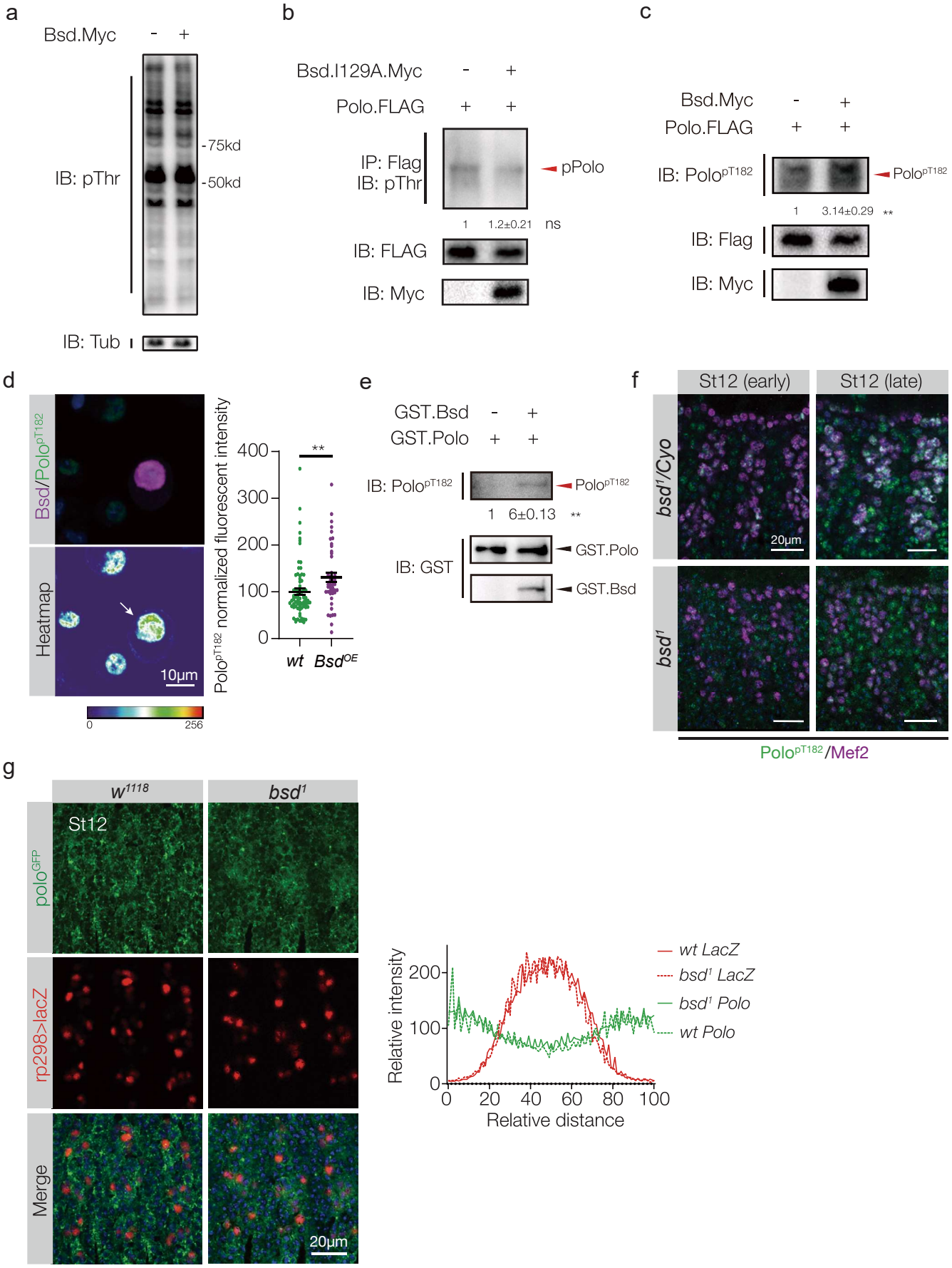

Figure S4, related to Figure 4. (A) Lysates from S2 cells transfected with a control plasmid or a plasmid expressing Bsd.Myc were immunoblotted with anti-phosphothreonine (pThr). Lysates showed equivalent levels of pThr. (B) Lysates from S2 cells transfected with Polo and a control plasmid or Bsd.I129A were immunoblotted with pThr. The amount of phosphorylated Polo was not significantly different between cells transfected with Bsd.I129A and controls. (C) Lysates from S2 cells transfected with Polo and a control plasmid or wild-type Bsd were immunoblotted with anti-PLK1-phospho-T210 ($Polo^{pT182}$). There was a significant increase in the amount of phosphorylated Polo in cells transfected with Bsd compared to controls. (D) S2 cells transfected with Bsd.Myc and Polo, immunolabeled for pThr210-PLK1 ($Polo^{pT182}$ green) and Myc (red). Bsd transfected cells (arrows) showed significantly more $Polo^{pT182}$ than controls. (E) Purified GST-Bsd and GST-Polo were used for cell free *in vitro kinase* assays. $Polo^{pT182}$ was detected by immunoblotting with anti-pThr210-PLK1 antibody. Bsd directly phosphorylated Polo. (F) Early and late Stage 12 embryos immunolabeled for activated $Polo^{pT182}$ (green) and Mef2 (violet). $Polo^{pT182}$ increased during Stage 12 in control (*bsd*^{1} heterozygous) but not *bsd*^{1} embryos. Control and *bsd*^{1} embryos were labeled in the same preparation. (G) Stage 12 embryos with endogenous GFP-tagged Polo (*Polo*^{GFP}) that expressed *rP298.nLacZ* were immunolabeled for GFP (green) and lacZ (red). Fluorescent intensity and cellular localization of total Polo protein was comparable between control and *bsd*^{1} embryos. Graph plots Polo and nlacZ fluorescent intensity across myoblasts (n≥32 cells from 6 or more embryos per genotype). Significance was determined by unpaired student's t test (B-D). (ns) not significant, **($p<0.01$), ***($p<0.0001$),****($p<0.0001$). Error bars represent SEM.

Figure S5, related to Figure 5

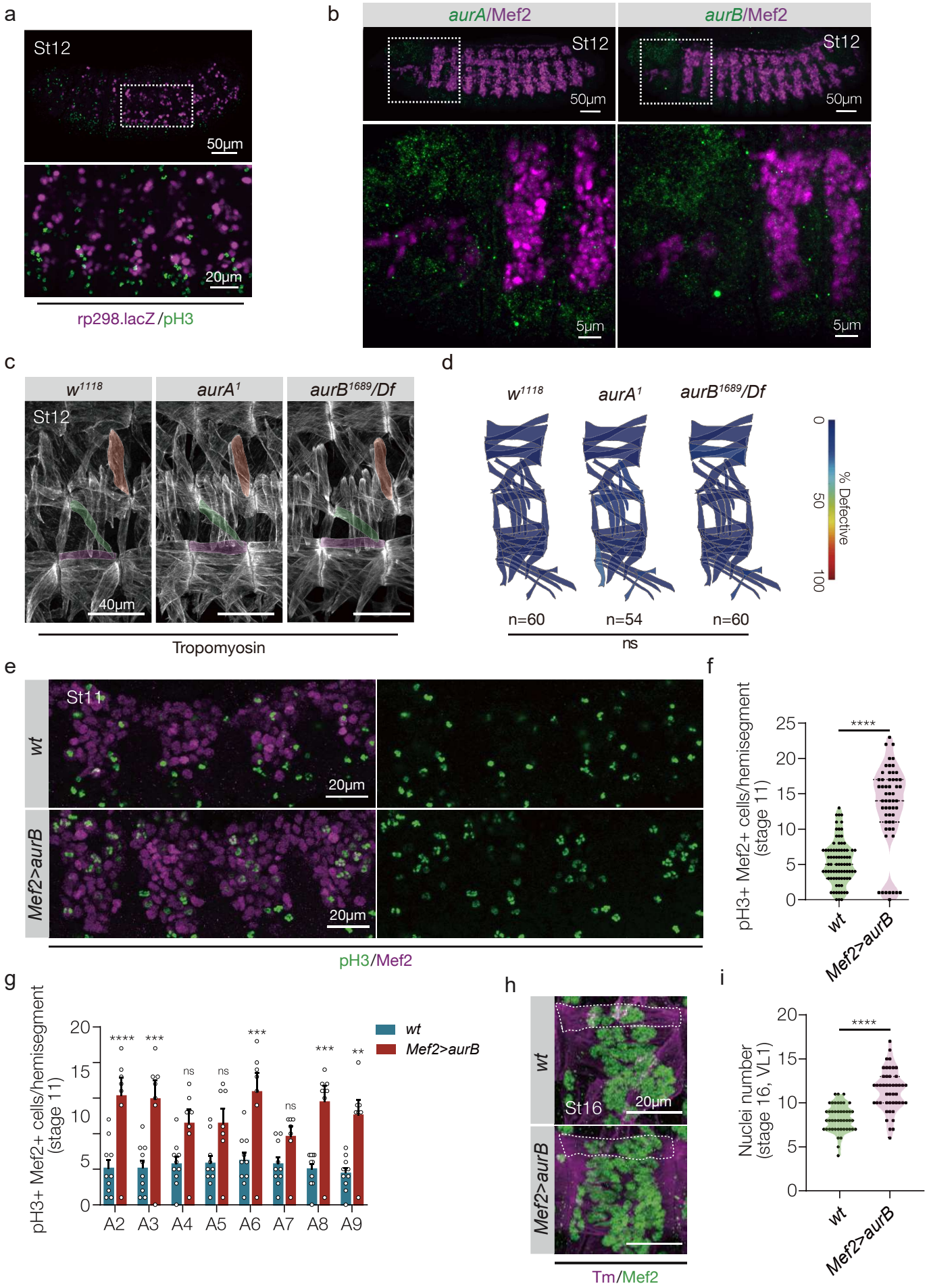

Figure S5, related to Figure 5. (A) Stage 12 *rP298.nLacZ* embryo immunolabeled for phosphorylated Histone 3 (pH3, green) and lacZ (violet). lacZ expressing nascent myotubes were not pH3 positive. (B) Stage 12 embryos labeled for *aurA* (left, green), *aurB* (right, green) and Mef2 (violet). *aurA* and *aurB* expression was excluded from the somatic mesoderm in Stage 12 embryos. (C) Stage 16 embryos labeled with Tropomyosin. DT1, LO1, and VL1 muscles are pseudocolored orange, green, and violet. Muscle patterning was unaffected in $aurA^{1}$ and $aurB^{1689}$*/Df(3L)BSC447* embryos. (D) Quantification of muscle phenotypes, as described in Fig. 1B. (E) Stage 11 embryos immunolabeled for pH3 (green) and Mef2 (violet). *Mef2>aurB* embryos had significantly more pH3/Mef2 double positive cells than control embryos. n≥7 embryos per genotype. (F) Quantification of pH3/Mef2 double positive cells in (E). Each data point represents a single hemisegment. (G) Quantification of pH3/Mef2 double positive cells in (E), grouped by hemisegment (A2-A9). (H) Stage 16 embryos immunolabeled for Mef2 (green) and Tropomyosin (violet). (I) Myotubes in *Mef2>aurB* embryos had significantly more myonuclei than control embryos. n=6 embryos per genotype. Significance was determined by Fisher's exact test (C), unpaired student's t test (E,H), and two-way ANOVA (F).

Figure S6, related to Figure 6

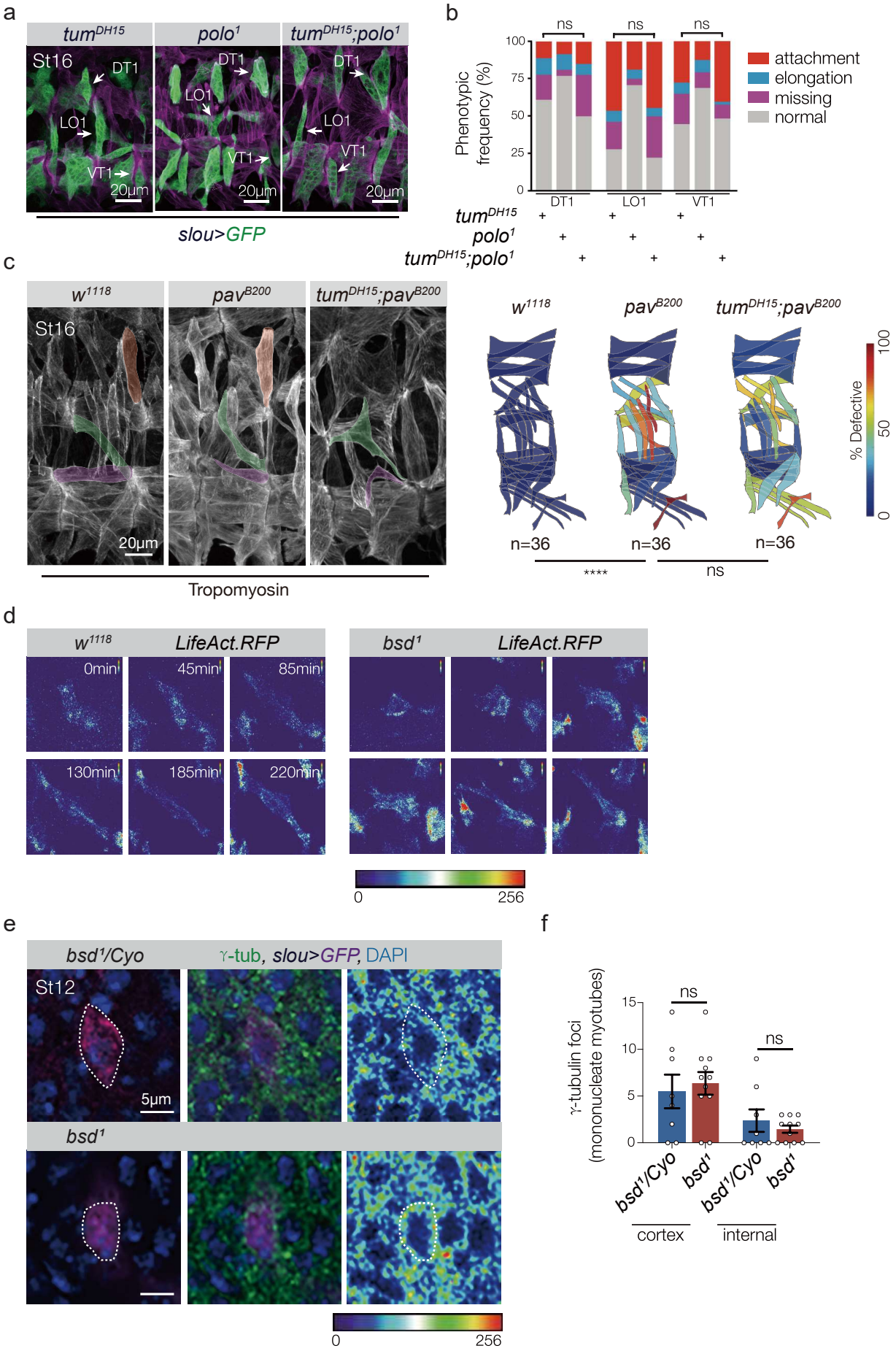

Figure S6, related to Figure 6. (A) Stage 16 embryos labeled for *slou>GFP* (green) and Tropomyosin (violet). DT1, LO1, and VT1 muscle patterning was disrupted in tum^{DH15}, $polo^{1}$, and tum^{DH15} $polo^{1}$ embryos. (B) Histogram of DT1, LO1, and VT1 phenotypes. The frequency of muscle phenotypes was not significantly different between tum^{DH15} embryos and tum^{DH15} $polo^{1}$ double mutant embryos. n≥54 hemisegments per genotype. (C) Stage 16 embryos labeled with Tropomyosin. DT1, LO1, and VL1 muscles are pseudocolored orange, green, and violet. The muscle pattern was disorganized in pav^{B200} embryos, but the frequency of muscle phenotypes was not significantly different between pav^{B200} embryos and tum^{DH15} pav^{B200} embryos. n=36 hemisegments per genotype. Quantification of muscle phenotypes is as described in Fig. 1B. (D) LO1 myotubes from (Fig. 6C) showing F-actin expression by heat map. Scale bar represents the detection range. F-actin levels were equivalent between control and bsd^{1} myotubes. (E) Mononucleate LO1 myotubes from Stage 12 *slou>GFP* embryos labeled for γ-tubulin (green), GFP (violet) and DAPI (blue). Mononucleate, polarized myotubes have just initiated myotube guidance (see Movie 1). Control (bsd^{1}/Cyo) myotubes showed only cortical γ-tubulin foci. bsd^{1} myotubes had an equivalent number of cortical γ-tubulin foci compared to controls. (F) Quantification of γ-tubulin foci in mononucleate Stage 12 myotubes. Embryos used for (E,F) were derived from the same preparation. n=5 embryos per genotype. Significance was determined by Fisher's exact test (B,C), unpaired student's t test (F). (ns) not significant, ****($p<0.0001$). Error bars represent SEM.

Figure S7. Related to Figure 7

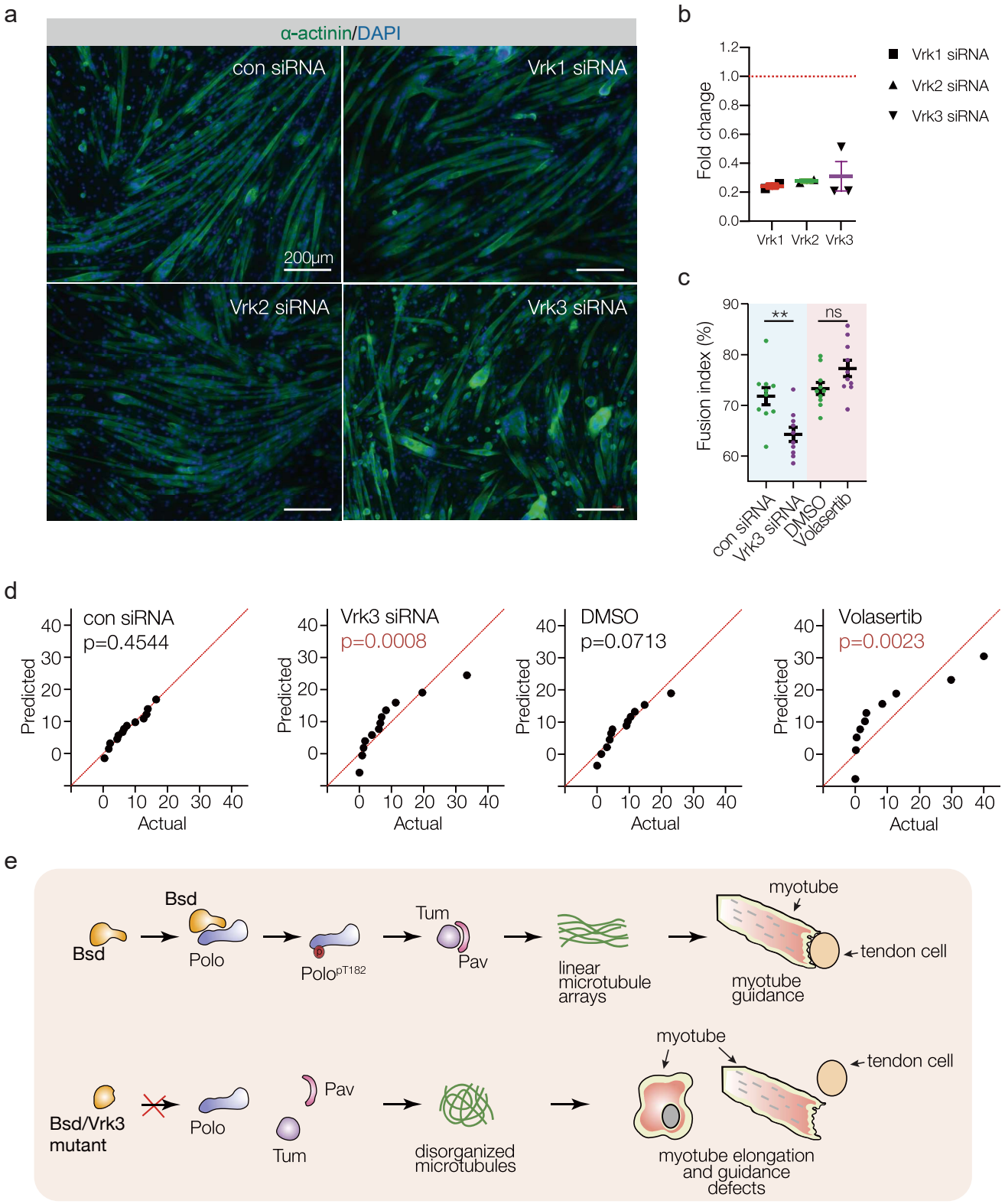

Figure S7, related to Figure 7. (A) C2C12 cells treated with control (scrambled) siRNA or a cocktail of two siRNAs against murine Vrk1, Vrk2, or Vrk3. Cells were fixed after 7 days in differentiation media and labeled for α-actinin (green) to detect differentiated myotubes and DAPI (blue). Vrk3 knockdown myotubes were shorter than controls and often rounded. Vrk1 and Vrk2 knockdown myotubes were indistinguishable from control cells. (B) Quantitative real time PCR of siRNA treated C2C12 cells. Fold change is relative to control treated cells (red line). (C) Myoblast fusion index shows reduced fusion in Vrk3 siRNA treated C2C12 cells. (D) QQ plot of myotube length distribution, related to Figure 7C. Each data point represents the actual length distribution value (x) and the predicted length value for a normal distribution (y). The lengths of the con siRNA and DMSO treated myotubes fit the normal distribution; the lengths of the Vrk3 siRNA and Volasertib treated myotubes did not fit the normal distribution. (E) Model of Bsd and the Polo/Tum/Pav cytoskeletal regulatory module. Bsd reorganizes the microtubule cytoskeleton to direct myotube guidance, and likely acts through Tum and Pav. Significance was determined by unpaired student's t-test (C) and D'Agostino & Pearson test (D). (ns) not significant, **($p<0.01$), ****($p<0.0001$). Error bars represent SEM.